Coupled rate and transport equations modeling proportionality of light yield in high-energy electron tracks: CsI at 295 K and 100 K; CsI:Tl at 295 K

Xinfu Lu,[1] Qi Li,[1] G. A. Bizarri,[2] Kan Yang,[3] M. R. Mayhugh,[3,*] P. R. Menge,[3] and R. T. Williams[1,†]

[1]*Wake Forest University, Department of Physics, Winston Salem, North Carolina 27109, USA*

[2]*Lawrence Berkeley National Laboratory, Berkeley, California 94720, USA*

[3]*Saint-Gobain Crystals, Hiram, Ohio 44234, USA*

(Received 30 June 2015; revised manuscript received 3 September 2015; published 24 September 2015)

A high-energy electron in condensed matter deposits energy by creation of electron-hole pairs whose density generally increases as the electron slows, reaching the order of 10^{20} eh/cm^3 near the end of its track. The subsequent interactions of the electrons and holes include nonlinear rate terms and transport as first hot and then thermalized carriers in the nanometer-scale radial dimension of the track. Charge separation and strong radial electric fields occur in a material such as CsI with contrasting diffusion rates of self-trapped holes and hot electrons. Eventual radiative recombination has a nonlinear relation to the primary electron energy because of these interactions. This so-called intrinsic nonproportionality of electron response limits the achievable energy resolution of a given scintillation radiation detector material. We use a system of coupled transport and rate equations to describe a pure host (three equations) and one dopant (four more equations per dopant). Applying it first to the experimentally well-characterized system of CsI and CsI:Tl in this work, we use results of picosecond absorption spectroscopy, interband Z-scan measurements of nonlinear rate constants, and other experiments and calculations to determine most of the more than 20 rate and transport coefficients required for modeling. The model is solved in a track environment approximated as cylindrical and is compared to the proportionality curve and total light yield of undoped CsI at temperatures of 295 and 100 K, as well as thallium dopant in CsI:Tl at 295 K. With this degree of validation, the space and time distributions of carriers and excitons, both untrapped and trapped, are examined within the model to gain an understanding of the main competitions controlling the nonproportionality of response.

DOI: 10.1103/PhysRevB.92.115207 PACS number(s): 78.70.Ps, 72.20.Jv, 78.55.−m, 78.20.Bh

I. INTRODUCTION

Gamma rays deposit energy in radiation detectors along ionized tracks left by energetic electrons or positrons from photoelectric, Compton scattering, and pair-production interactions. If there exists a known relation between the detector output and the energy of the primary particle, the detector is spectroscopic. In scintillation detectors, the response is the number of detected photons resulting from stopping of the primary particle. If the scintillator's intrinsic response is not proportional to the particle energy, this so-called intrinsic nonproportionality combined with random fluctuations in electron energies produced by scattering of gamma rays contributes to the degradation of energy resolution in gamma detectors. As electrons slow down, their energy deposited per unit length, dE/dx, rises toward a maximum near 50 eV. This variable energy deposition along the length of the main track and any branches has long been considered to be a factor in the observed nonproportionality between light yield and radiation energy in scintillators. In the last ten years particularly, the effort to understand and control nonproportionality has increased with the objective of improving the gamma energy resolution for a variety of practical applications [1–4].

The experimental tools brought to bear have become more sophisticated. The accurate measurement of light-yield produced by internally generated electrons over a wide range of energies by the Compton-coincidence [5,6] and K-dip [7] methods is one example. The use of pulsed lasers to measure transient behavior in the picosecond regime [8] and to induce specific ionization densities allowing measurement of nonlinear processes at carrier densities found in the gamma ray induced electron tracks [9] is another. There has been commensurate progress in the theoretical understanding of energy deposition and subsequent transport and recombination along the ionized tracks [10–18].

Since about 2010, we have been developing and testing a scintillation response model of progressive comprehensiveness that computes emission intensity over time and space in electron tracks by solving coupled rate and transport equations describing both the movement and the linear and nonlinear interactions of the charge carriers deposited along the ionized track [19–21]. The tracks are initially very narrow before hot and thermalized carrier diffusion takes effect, with a radius estimated as about 3 nm in NaI from the hole thermalization range [13], experiments on nonlinear quenching rate [9], and Monte Carlo simulations [22]. A similar size of the initial radius is indicated in other scintillators [23]. Even after hot and thermalized carrier diffusion, the radius is much less than the track length of several μm for 20 keV up to nearly a millimeter for 662 keV, which suggests that a good representation can be obtained by modeling diffusion in one dimension, the radial one. The track is numerically chopped into cells small enough to approximate their ionization density as constant and these form the individual parts of a finite element model. The initial ionization density values vary from cell to cell along the length of the track with the variation in dE/dx and we calculate the light yield for each local value of dE/dx. This intermediate quantity that we call local light yield as a function of dE/dx

*Currently: Faceted Development, LLC.

†williams@wfu.edu

cannot itself be directly measured by experiments. The local light yields must be multiplied by the number of times the associated ionization density occurs in repeated simulations (e.g., using GEANT4 [24,25]) for the given initial electron energy, and then the yields are summed to report the total light yield. When this calculation is carried out over a range of energies, the results give the predicted electron energy response or proportionality curve as a function of the initial electron energy for comparison to Compton-coincidence and K-dip experiments. We are not restricting the electron tracks modeled to be single linear tracks. Delta rays and high-energy Auger spurs are represented within the GEANT4 simulations, which determine the weighting of each part of our modeled local light yield function (light yield versus excitation density) in the final tally of electron response. The computation of local light yield takes account of the initially hot electrons and their thermalization, the hole self-trapping if it occurs in the material, the electron, hole, and exciton diffusion, the electrostatic attraction of electrons and holes if there is charge separation, the second- and third-order nonlinear quenching when ionization density is high enough, and the carrier trapping with and without luminescence. The equations embodying the local light yield model are presented in Sec. II.

In this paper, the model's ability to compute nonproportionality is tested in three steps. First, the proportionality curve is calculated and fit to the response for undoped CsI at room temperature. Next, the host parameters considered to have the most important temperature dependence are adjusted only for temperature according to experiment and/or theoretical temperature-dependence trends, and comparison is made to the gamma yield proportionality data for undoped CsI near 100 K published by Moszynski *et al.* [26]. Finally, Tl is added at room temperature using the additional equations and dopant parameters needed for modeling, but the host parameter values are kept at those determined from literature and fitting of the undoped CsI.

II. THE MODEL AND ITS NUMERICAL SOLUTION IN ELECTRON TRACKS

A. Ionization density, local light yield, and distribution of dE/dx

The rate equations we are solving are expressed in terms of excitation density n. A radial dimension is needed together with length x along the track in order to convert a given dE/dx to an initial excitation density profile. We assume a Gaussian cylindrical distribution of excitations, and the Gaussian radius is used to convert dE/dx (eV/cm) to volume-normalized local initial excitation density $n(r,t=0)$ (excitations/cm^3). The calculation of local light yield in terms of the volume-normalized excitation density n rather than the linear energy deposition dE/dx is an important characteristic of this model. The volume-normalized density can be dramatically altered by diffusion as time progresses during the development of the light pulse. Rate terms dependent on products of local electron and hole volumetric densities such as exciton formation and Auger decay will be curtailed at lower densities after diffusion, or even terminated to the extent that charge separation occurs by hot-electron diffusion against hole self-trapping.

The calculation of response versus electron energy has two parts: (1) the solution of coupled diffusion-limited rate equations in a spatial track geometry approximated as cylindrical for one given on-axis excitation density, evaluating radiative and nonradiative recombination events and trapping in each cell and time step. The time- and space-integrated radiative recombination events are tabulated as a function of the initial on-axis excitation density. When normalized by the total number of electron-hole pairs produced at that excitation density, this quantity is what we have termed local light yield. (2) The results of Monte Carlo simulations of the linear energy deposition rate dE/dx during stopping of an electron of initial energy E_i using the GEANT4 code [24] are averaged over multiple simulations to calculate the distributions of the probability that an electron of initial energy E_i will produce each local energy deposition rate dE/dx. We multiply the local light yield $Y_L(n_0)$ by the probability $P(n_0,E_i)$ of occurrence of each initial on-axis local density n_0 in the stopping of an electron of initial energy E_i. Integration of $Y_L(n_0)\,P(n_0,E_i)$ over all n_0 yields the electron energy response or integrated light yield as a function of the initial energy of an electron launched internally within the sample [27]. The experimental electron energy response is typically measured by the Compton-coincidence [5,6] or K-dip [7] techniques. By convention, the experimental electron energy response is usually normalized to unity at 662 keV.

B. Coupled system of diffusion-limited rate equations for local light yield versus on-axis initial excitation densities in the electron track

The local light yield in our model for an undoped scintillator and one doped with a single activator is calculated using Eqs. (1)–(7):

$$\frac{dn_e}{dt} = G_e + D_e\nabla^2 n_e + \mu_e\nabla\cdot n_e\vec{E} - (K_{1e}+S_{1e})n_e - Bn_en_h - B_{ht}n_en_{ht} - K_3n_en_en_h - K_3n_en_en_{ht}, \quad (1)$$

$$\frac{dn_h}{dt} = G_h + D_h\nabla^2 n_h - \mu_h\nabla\cdot n_h\vec{E} - (K_{1h}+S_{1h})n_h - Bn_en_h - B_{et}n_{et}n_h - K_3n_en_en_h - K_3n_en_{et}n_h, \quad (2)$$

$$\frac{dN}{dt} = G_E + D_E\nabla^2 N - R_{1E}N - (S_{1E}+K_{1E})N + Bn_en_h - K_{2E}N^2, \quad (3)$$

$$\frac{dn_{et}}{dt} = D_{et}\nabla^2 n_{et} + \mu_{et}\nabla\cdot n_{et}\vec{E} + S_{1e}n_e - K_{1et}n_{et} - B_{et}n_{et}n_h - B_{tt}n_{et}n_{ht} - K_3n_en_{et}n_h, \quad (4)$$

$$\frac{dn_{ht}}{dt} = S_{1h}n_h - B_{ht}n_en_{ht} - B_{tt}n_{et}n_{ht} - K_3n_en_en_{ht} \quad (5)$$

$$\frac{dN_t}{dt} = S_{1E}N + B_{ht}n_en_{ht} + B_{et}n_{et}n_h + B_{tt}n_{et}n_{ht} - R_{1Et}N_t - K_{2Et}N_t^2, \quad (6)$$

$$S_{1x} = \frac{n_{Tl^+}}{n^0_{Tl^+}}S^0_{1x}, \text{ where } n_{Tl^+} = n^0_{Tl^+} - n_{et} - n_{ht} - N_t. \quad (7)$$

We will now describe each of the terms in the above equations and mention their significance in selected cases. The electron and hole equations (1) and (2) for carrier densities n_e and n_h are of identical form, so we discuss them together. The first term in equations (1) and (2), $G_{e,h}$, is the generation term specifying the initial Gaussian radial profile at $t = 0$. The Gaussian track radius of 3 nm is discussed along with its justification in Sec. IV, which includes parameter values. The magnitude of $G_{e,h}(r = 0)$ is the on-axis excitation density

$$n_0 = \frac{dE/dx}{\pi r_{\text{track}}^2 \beta E_{\text{gap}}}. \tag{8}$$

Next in Eqs. (1) and (2) are the carrier diffusion terms. In alkali halides including CsI, the hole is self-trapped very quickly [13,28,29]. In quantum molecular dynamics calculations for NaI [30], hole self-trapping is indicated to occur as fast as 50 femtoseconds at room temperature. In view of such rapid self-trapping, the hole equation (2) is simply written in terms of the density of self-trapped holes, n_h, diffusing with the hopping diffusion coefficient of self-trapped holes. This effectively ignores the first 50 fs of hole evolution, except as it may be represented in the initial Tl^{++} production G_{ht} in thallium-doped CsI. [31,32]. However, we cannot ignore the early evolution of the electrons. The cooling of hot electrons is rather slow in CsI (∼4-ps mean thermalization time) [10] due to its low optical phonon frequency. D_e is a function of electron temperature T_e and therefore a function of time during the electron cooling process, $D_e(T_e(t))$. The determination of the hot electron diffusion coefficient in this work relies on the calculations of Wang *et al.* [10] on the hot electron range in CsI, as described in Sec. IV. The great difference in the diffusion ranges of hot electrons and self-trapped holes in alkali halides means that electrons and holes are quickly separated as will be seen directly in the radial distributions as a function of time. This is a significant factor affecting the various second- and third-order rate terms in Eqs. (1)–(6) that depend on the overlap of the electron and hole populations.

The third terms in Eqs. (1) and (2) represent the electric field driven currents. The tendency for separation of charge between hot electrons and relatively immobile self-trapped holes in the alkali halides means that large radial electric fields can arise and will tend to drive the corresponding radial currents. The displacement of a given electron imparted by any reasonable space-charge electric field between electron-phonon scattering events is much smaller than the displacement due to the kinetic energy of a hot (e.g., 3 eV) electron between the same scattering events. So, initially, the hot electrons run outward to a radial distribution peak shown to be about 50 nm in CsI (with a tail extending as far as 200 nm) [10], leaving behind self-trapped holes (STH) in a cylinder with radius about 3 nm [9,13,22]. As the electrons cool to the thermalized energy near the conduction band minimum, the hot diffusion coefficient drops toward the smaller thermalized diffusion coefficient D_e and the electric field term can finally assert itself as stronger than the diffusion term. At that point, the direction of electron current reverses from outward to inward as thermalized conduction electrons in the undoped pure material are collected back toward the line charge STH where recombination can occur. In an activated scintillator such as CsI:Tl, a similar process occurs but on a much slower time scale set by the hopping diffusion of electrons trapped on thallium as they are drawn back toward a charged core of Tl^{++} ions, and as the STH diffuse out to find Tl^0.

The fourth terms in Eqs. (1) and (2) represent carrier capture on deep defect traps with rate constants $K_{1e,h}$ and on the activator dopant with rate constants $S_{1e,h}$. The symbol K was chosen for representing killing of the radiative probability when a carrier is caught on a deep defect trap. The symbol S was chosen to represent the concept that trapping on the activator represents storage of the carrier for possible radiative emission through the activator-trapped exciton equation (6). The first-order rate constants for capture are proportional to the respective trap concentration, so, for example, if there is no activator, the rate constants $S_{1e,h}$ coupling free carriers into the trapped-carrier and trapped-exciton equations (4)–(6) vanish, and the model automatically reduces just to Eqs. (1)–(3) for a pure material.

The fifth terms in Eqs. (1) and (2) are the bimolecular exciton formation rates characterized by rate constant B and proportional to the product of electron and hole densities at a given location and time. This term can vanish due to charge separation of hot electrons from STH, but the bimolecular rate of exciton formation will come into play later as thermalized carriers are united in their mutual space-charge field. The exciton formation rate, $-B_{n_e n_h}$, is a loss term for Eqs. (1) and (2) but it is the main source term in Eq. (3) governing exciton density N.

The sixth terms in Eqs. (1) and (2) are the bimolecular rates of forming trapped excitons from capture of one free carrier on a trap (activator in the case considered) already occupied by the other carrier. Similar to the commentary immediately above, this is a loss term for the free carrier density but a source term in Eq. (6) for trapped excitons on the activator at density N_t.

The seventh terms in Eqs. (1) and (2) are the third-order Auger recombination rates of free carriers. McAllister *et al.* [33] found that in NaI, the valence-band structure does not have states to receive the excited spectator hole in an $n_e n_h n_h$ Auger process. The valence-band structure of CsI seems to support the same conclusion. Therefore we retain only the Auger rate term of the form $K_3 n_e n_h n_e$ in this work. The Auger rate constant in CsI has been measured by interband Z-scan experiments [9]. The excitation density gradient and consequent charge separation experienced in the laser Z-scan experiment are significantly less than in an electron track. This renders K_3 more readily measurable by laser Z scan, whereas the charge separation phenomenon in an alkali halide can act to severely limit the importance of free-carrier Auger recombination in tracks excited by high-energy electrons. The eighth terms in Eqs. (1) and (2) are similar Auger terms in which one of the carriers already occupies the activator dopant.

There are other rate terms that could be included in the free carrier equations. Examples would be source terms due to thermal ionization of shallow and deep traps. Thermal ionization of deep traps is omitted if the time for release is longer than usual scintillator gate times of the order of 5 μs, because the study of afterglow is beyond what we want to tackle during the first tests of this model. Ionization from

known shallow traps, specifically electron release from Tl^0 in CsI:Tl, is included effectively in this system of equations in a way that will be discussed during the description of the trapped carrier equations (4)–(6) below.

Equation (3) for the density of excitons, N, has no source term other than the bimolecular exciton formation transferring population from the free carrier equations, because of our setting $G_E = 0$ for reasons discussed in relation to Table I, Sec. IV. Similar to our earlier discussion regarding the holes as immediately self-trapped in an alkali halide, the excitons represented by N in Eq. (3) are regarded as self-trapped excitons (STE) when alkali halides are the materials of interest. Their diffusion, by thermally activated hopping/reorientation [16,34,35], is represented by the second term. The third term in Eq. (3) is the radiative decay rate. This is the only rate term that produces light in the first three equations for a pure material. In the case of pure CsI, R_{1E} is the reciprocal of the radiative lifetime of the 3.7-eV Type-II STE at 100 K, and of the 4.1-eV luminescence of the equilibrated Type-I and -II STEs at room temperature identified by Nishimura *et al.* [36]. The fourth term in Eq. (3) is a linear loss term from the exciton population involving two rate constants. The S_{1E} rate constant represents linear trapping of STEs on a Tl^+ activator (if present) and is therefore an energy storage term that can contribute ultimately to the Tl^{+*} activator luminescence via Eq. (6) while subtracting from the intrinsic STE luminescence in Eq. (3). The K_{1E} linear loss rate constant is used to describe the dominant path of quenching STE luminescence at room temperature, which in many alkali halides is the nonradiative thermally activated crossing to the ground state. The fifth term in Eq. (3) is the bimolecular source term due to exciton formation from free carriers. The final term represents second-order dipole-dipole quenching of STEs.

Equations (4)–(6) describe populations of trapped electrons, holes, and excitons, respectively, on the activator dopant, in this case, Tl^+ substituting for Cs^+. Without going through all the rate and transport coefficient symbol names again, we comment generally that the carrier/exciton densities, the rate constants, and the transport coefficients carry the same symbols as in Eqs. (1)–(3) to indicate corresponding physical quantities, except now the fact of being trapped on the activator is indicated by the subscript "t" on all such terms. To illustrate the meaning of a few of the trapped carrier/exciton terms, for example, $+S_{1e}n_e$ is the rate of trapping thermalized electrons on the activator dopant, $-B_{et}n_{et}n_h$ is the bimolecular rate of converting trapped electron population, n_{et}, into trapped excitons feeding the corresponding source term in Eq. (6), and $-K_3n_en_{et}n_h$ is the rate of Auger recombination involving a trapped electron and free electrons and holes. $-R_{1Et}N_t$ is the first-order radiative rate of decay of dopant-trapped excitons at density N_t, and $-K_{2Et}N_t^2$ is the rate of second-order dipole-dipole quenching of two trapped excitons.

The terms in Eq. (4) representing diffusion of trapped electrons, $D_{et}\nabla^2 n_{et}$, current in a field, $\mu_{et}\nabla\cdot n_{et}\vec{E}$, and implied motion of the trapped electrons in bimolecular recombination with immobile holes trapped as Tl^{++} in the term $B_{tt}n_{et}n_{ht}$ deserve special comment. These terms account for thermal untrapping from shallow traps even though no explicit untrapping rate is represented in Eqs. (1)–(6). The following two equations would replace Eqs. (1) and (4) above if we were to explicitly represent untrapping and retrapping of electrons on thallium in CsI:Tl:

$$\frac{dn_e}{dt} = G_e + U_{et}n_{et} + D_e\nabla^2 n_e + \mu_e\nabla\cdot n_e\vec{E} - (K_{1e}+S_{1e})n_e - Bn_en_h - B_{ht}n_en_{ht} - K_3n_en_en_h - K_3n_en_en_{ht}, \quad (1a)$$

$$\frac{dn_{et}}{dt} = S_{1e}n_e - U_{et}n_{et} - B_{et}n_{et}n_h - K_3n_en_{et}n_h. \quad (4a)$$

In these equations, the untrapping loss term $-U_{et}n_{et}$ in Eq. (4a) for electrons trapped as Tl^0 is an added positive source term after G_e in Eq. (1a) for free electrons. There are now no diffusion or electric current terms in Eq. (4a) because all of the transport occurs while the electrons are free and therefore accounted for in Eq. (1a). Likewise, the term $-B_{tt}n_{et}n_{ht}$ introduced in Eq. (4) to represent the bimolecular recombination of thallium-trapped electrons with thallium-trapped holes is absent in Eq. (4a) because such processes formally take place through the term $-B_{ht}n_en_{ht}$ in the free-electron equation during the time that the electron is untrapped from Tl^0. In such a description, Eqs. (5) and (6) would also be without the B_{tt} terms. However, although the equations themselves are simpler in this physically realistic formulation, their numerical solution spanning time scales from femtoseconds to microseconds presents computational difficulties. In fact we coded the model first for the equation set with Eqs. (1a) and (4a) in place of Eqs. (1) and (4), as well as the modification of Eqs. (5) and (6), and ran the first calculation of local light yield. It took an unacceptably long time.

Calculating the outcomes of the free-carrier equations (1) and (2) requires time steps as short as 0.1 femtosecond in the finite element method. Calculating the outcomes of the trapped carrier equations (4a)–(6a) on the other hand requires calculations running out to at least 5 microseconds. Calculations spanning such time ranges were made manageable in terms of computer time by varying the time steps progressively longer from beginning to end when thermal untrapping of carriers was not included. It worked because as time went on, the free carriers were trapped or were combined as self-trapped excitons, and then larger time steps could be used. We used the forward-time central-space (FTCS) method of Rectenwald [37] in setting time steps, such that the maximum change of electron, hole, or exciton density in a time step would not exceed 10%. (5% and 20% limits were tried with essentially the same result.) However, if thermal release of trapped carriers is included directly, then continual reinjection of free carriers occurs over long time scales, so that short time steps continue to be needed to accurately determine the fate of the fresh free electrons via Eq. (1a). This leads to the unacceptably long computational times just mentioned.

Computational economy for CsI:Tl was achieved by noting the following approximate equivalency. In a CsI crystal doped with Tl^+ at 0.082 mole%, the capture (and recapture) rate constant for electrons on Tl^+ is $S_{1e} = 3.3\times10^{11}\text{s}^{-1}$ as directly measured by picosecond spectroscopy (see Sec. IV, Table I). This is the highest linear capture rate constant of all those listed in Table I. The measured rate constant for thermal

TABLE I. Parameters (and their literature references or comments on methods) as used for the calculation of proportionality and light yield in undoped CsI at 295 K.

Parameter	Value	Units	Publ/Est	Refs. and notes
r_{track}	3	nm	3,3,2.8	Refs. [9,13,22] for NaI
βE_{gap}	8.9	$(eV/e\text{-}h)_{\text{avg}}$	8.9	Ref. [26] CsI 100 K LY 112 000 ph/MeV
ϵ_0	5.65	N/A	5.65	Refs. [47,48]
μ_e	8	cm^2/Vs	8	Ref. [49]
D_e	0.2	cm^2/s	0.2	$D = \mu kT/e$
μ_h	10^{-4}	cm^2/Vs	10^{-4}	$D_h = \mu_{hkT/e}$, Ref. [16]
D_h	2.6×10^{-6}	cm^2/s	2.6×10^{-6}	Ref. [16,34]
D_E	2.6×10^{-6}	cm^2/s	2.6×10^{-6}	$D_{\text{STE}} \approx D_{\text{STH}}$, Ref. [50]
$B(t > \tau_{\text{hot}})$	2.5×10^{-7}	cm^3/s	2.5×10^{-7}	Ref. [8]
K_3	4.5×10^{-29}	cm^6/s	4.5×10^{-29}	Ref. [9]
K_{2E}	0.8×10^{-15}	$\text{t}^{-1/2}\text{cm}^3\text{s}^{-1/2}$	0.8×10^{-15}	Ref. [9]
R_{1E}	6.7×10^6	s^{-1}	6.7×10^6	Ref. [36] and Eqs. (8) and (9) for R_{1E} and K_{1E}
K_{1E}	6×10^7	s^{-1}	6×10^7	solve model 662 keV for 2 ph/keV, Ref. [51]
τ_{hot}	4	ps	4	Ref. [10]
r_{hot} (peak)	50	nm	50	Ref. [10]
$D_e(t < \tau_{\text{hot}})$	3.1	cm^2/s		to reproduce $r_{\text{hot}}(peak) at \tau_{\text{hot}}$
S_{1e}	0	s^{-1}	0	zero in undoped host
S_{1h}	0	s^{-1}	0	zero in undoped host
S_{1E}	0	s^{-1}	0	zero in undoped host
$G_E(r = 0)$	0	cm^{-3}	$4\% G_e \rightarrow 0$	Refs. [52–54]
K_{1e}	2.7×10^{10}	s^{-1}		fitting variable No. 1, CsI proportionality
K_{1h}	0	s^{-1}	$10^{-5} K_{1e}$	ratio to K_{1e} based on Eq. (11)
E_i(norm)	200	keV		fitting variable No. 2, normalization

untrapping of electrons from Tl^0 at room temperature is $U_{et} = 7.1 \times 10^5\ \text{s}^{-1}$ (Sec. IV, Table II). Thus after being trapped and mostly inactive for 1.4 μs, the electron becomes free for about 3 ps on average and is exposed to all the channels represented in Eq. (1) including diffusion and response to electric fields. However, after roughly 3 ps, the majority of such electrons that escape the various other interaction channels in Eq. (1) are trapped yet again on one of the many Tl^+ ions, and the cycle repeats. If the recapture is on a different Tl^+ than the original, the electron will have hopped (diffused). However, the end result is indistinguishable from an alternative version in which the Tl^0 itself hopped by trading places with a neighbor Tl^+. This can be treated as a type of transport of the Tl^0 itself if we are able to define effective transport coefficients. We note that the trapped electron (Tl^0) changes location and undergoes capture or recombination at the relative fractional yields given by the rate terms in Eq. (1) but at an average rate reduced by the ratio of its lifetime as a free electron to its lifetime as a trapped electron, $U_{et}/S_{1e} = 2.2 \times 10^{-6}$. We therefore replaced the formally correct trapping/untrapping equations (1a) and (4a) by Eqs. (1) and (4) given earlier in which the effective transport of Tl^0 (the activator charge state, not the physical atom) is represented with coefficients D_{et} and μ_{et} that are smaller by 2.2×10^{-6} than the free-electron coefficients D_e and μ_e. Other free-electron rate constants to which the cyclically trapped/untrapped electrons are exposed only 2.2×10^{-6} of the time are similarly assigned the identifying subscript t and scaled down by the fixed factor. These are the bimolecular exciton formation rate from momentarily untrapped electrons and holes, $-B_t n_{et} n_h$, and deep defect capture of such momentarily untrapped electrons, $K_{1et} n_{et}$. It is necessary to introduce additionally the term $B_{tt} n_{et} n_{ht}$ for creation of excited Tl^{+*} at a rate proportional to the local concentrations of $\text{Tl}^0(n_{et})$ and $\text{Tl}^{++}(n_{ht})$. In the specific case of CsI:Tl, the Tl^{++} trapped holes are so deep that n_{ht} diffusion is considered negligible on scintillation time scales. In exchange for the complexity of more transport and rate terms introduced, we have been able to drop the thermal untrapping term because that information is implicit in the scaled values of new transport and rate coefficients. The computational economy is that time steps in the finite element method can be conveniently lengthened as time progresses. The complexity of introducing more coefficients is not too cumbersome because they all scale by the common free/trapped time ratio relative to the free-electron transport and rate coefficients already determined. For the rest of this paper, we use Eqs. (1)–(7).

The seventh equation keeps track of the change in the concentration of available dopant traps in their initial charge state of Tl^+. For example, a lattice-neutral Tl^+ ion that trapped a free electron to become Tl^0 is not available to trap another electron in the same way until subsequent events return that dopant ion to its original Tl^+ charge state. The coupling rate constants $S_{1e}, S_{1h}, S_{1E} = S_{1x}$ for electrons, holes, and excitons on Tl^+ are themselves proportional to the dopant concentration in the available charge state Tl^+, so the capture rates that they govern will decrease as the local concentration of Tl^+ gets "used up" temporarily. This saturation can have the effect of contributing as one factor to the "roll-off" of local light yield at high excitation density (low electron energy). Gwin and Murray concluded that the activator concentration was not a dominant

TABLE II. Parameters (and literature references or estimation methods) projected to $T = 100$ K for use in Eqs. (1)–(3) to fit the undoped CsI proportionality and light yield at 100 K. All other parameters needed for Eqs. (1)–(3) were kept at their room-temperature value listed in Table I.

Parameter	Value	Units	Publ/Est	Refs .
μ_e	31	cm^2/Vs	31	based on Refs. [36,60]
D_e	0.27	cm^2/s	0.27	$D = \mu kT/e$
μ_h	2.2×10^{-11}	cm^2/Vs	2.2×10^{-11}	based on Refs. [34,35] eval. 100 K
D_h	1.9×10^{-13}	cm^2/s	1.9 x10^{-13}	$D = \mu kT/e$
D_E	1.9×10^{-13}	cm^2/s	1.9×10^{-13}	$D_{STE} \approx D_{STH}$ per Refs. [50,61]
R_{1E}	1.1×10^{6}	s^{-1}	1.1×10^{6}	Fig. 3 in Ref. [36] (100 K)
K_{1E}	0	s^{-1}	$<3 \times 10^{4}$	Ref. [55] STE thermal quench 100 K
K_{2E}	1.6×10^{-16}	$t^{-1/2}cm^3s^{-1/2}$	$0.164 \times 0.8 \times 10^{-15}$	scale from Z scan in Ref. [9] $R_{1E}(100)/R_{1E}(295) = 0.164$
K_{1e}	1.3×10^{9}	s^{-1}		9× below K_{1e}(295 K) - scale per Ref. [62]; 2.4× fewer defects
E_i(norm)	200	keV		cluster spatial distribution is the same as at 295 K
K_3	4.5×10^{-29}	cm^6/s		moderate T dependence [33] but charge separation limits Auger

effect in their experiments on CsI:Tl [38]. In other scintillators than CsI:Tl, there have been observed experimental activator concentration effects on proportionality, such as LSO:Ce [2] and YAP:Ce [39].

We have applied the system of equations just described to calculate electron response curves for comparison to three experimental measurements: electron response in undoped CsI and CsI:Tl at 295 K and gamma response of undoped CsI at 100 K [26]. The experimental data and superimposed model calculation of proportionality for the three experimental conditions are summarized in Fig. 1.

III. EXPERIMENTAL PROPORTIONALITY DATA

The purpose of this section is to describe the experimental data used to develop and verify the model. This is the experimental part of Fig. 1 just presented. We measured Compton-coincidence electron energy response for nominally pure CsI and for CsI:Tl (0.082 mole%) in the same apparatus in order to have a matched pair of data for the electron response of doped and undoped material at room temperature. Data for gamma ray energy response in undoped CsI at about 100 K are available from Moszynski *et al.* [26]. The model in this study calculates electron response, strictly speaking, so comparison with this 100 K gamma response data requires additional attention.

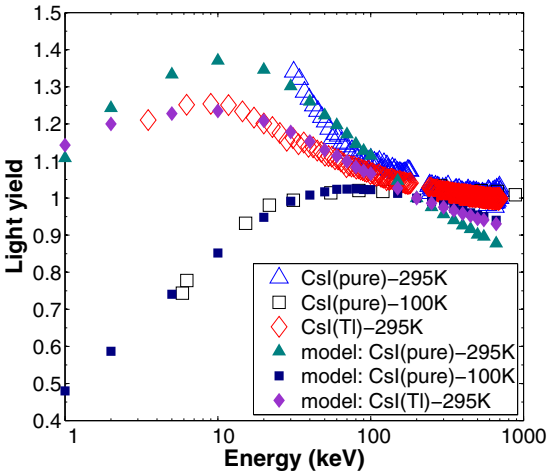

FIG. 1. (Color online) Combined plot of the three experiments and their model fits for undoped CsI (295 K), undoped CsI (100 K), and 0.082 mole% CsI:Tl (295 K). The "Energy (keV)" axis represents electron energy in the Compton coincidence measurements for CsI (295 K) and CsI:Tl (295 K) and gamma ray energy for CsI (100 K).

To measure scintillation light output proportionality, a Compton coincidence system [5] was set up according to the close-coupled design of Ugorowski [40]. Each crystal sample was coupled to a Hamamatsu R1306 photomultiplier (PMT) with optical grease. A Zn-65 source (1115.5 keV) was used to excite the crystals. An Ortec GMX-30200-P high-purity germanium (HPGe) detector was used to capture the Compton scattered gamma rays. Coincidence pulses from the HPGe and PMT detectors were recorded for periods of 30 minutes. Then ungated pulses were recorded for both PMT and HPGe for 5 minutes in between data acquisition in coincidence mode. The centroids of ungated pulse height spectra were continuously tracked to correct for drift of the gain in both detectors. Several cycles were run to reduce statistical uncertainty. Results at room temperature for doped and undoped CsI are shown in the upper two experimental curves of Fig. 1 above.

Moszynski *et al.* measured the gamma yield spectra of proportionality and the total light yield at 662 keV of two undoped CsI samples, CsI(A) and CsI(B), cooled to low temperature [26]. The samples were close-coupled to a large area silicon avalanche photodetector in a liquid nitrogen cryostat, which cooled the detector/sample assembly to a temperature characterized as about 100 K. Their sample B obtained from a university group had the higher light yield, which was measured to have the extraordinarily high value of 124 000 photons/MeV ±12 000 at the temperature of 100 K. Sample B at 100 K also produced a flatter proportionality curve at high energy, making it an interesting first target for comparisons to our model at low temperature. Sample A from a commercial supplier had lower light yield and displayed a more humped proportionality curve. Because the 100-K data were only available as a gamma response we also measured

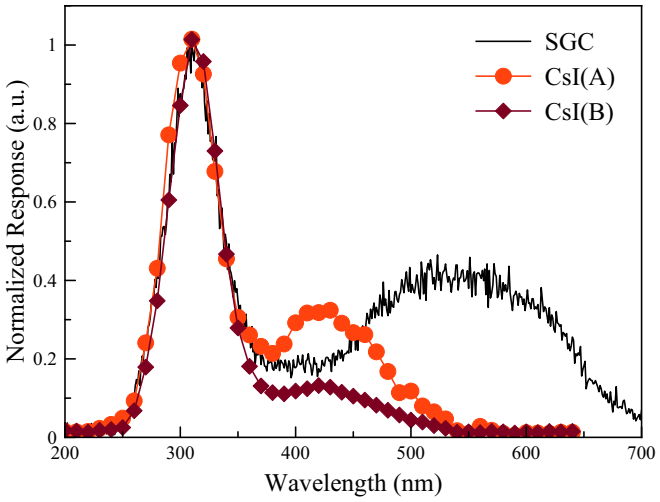

FIG. 2. (Color online) Radioluminescence spectra excited with Am-241 gamma rays at room temperature in the undoped sample (SGC unmarked, noisy line) compared with similar data extracted from Moszynski *et al.* [26] for CsI(A) (solid circles) and CsI(B) (solid diamonds)

the gamma response of our undoped and Tl doped samples as reported in Appendix B.

The differences between samples CsI(A) and CsI(B) in the Moszynski *et al.* [26] work motivated characterization and comparison of our undoped CsI sample with results shown in Fig. 2.

The figure shows that their samples and ours are similar in that they display a dominant uv radioluminescence peak near 310 nm at room temperature associated with fast emission but they differ in the amount of visible signal produced, in particular a band near 425 nm sometimes ascribed to vacancies [41,42] and associated with slow emission. CsI(B) had the least visible emission in this region, CsI(A) the most, and our sample an intermediate amount. Sample SGC also displayed substantially more emission toward the red but it was measured in a system with greater red sensitivity. Chemical analysis for 31 elements was performed by inductively coupled plasma-mass spectrometry (ICP-MS) on a slice taken from one end of the sample. Only iron at 0.003% was detected. Tl was <0.0005%. Sodium was not tested. The impurity analysis and optical absorption measurements given in Appendix C establish that the 550 nm emission is not due to Tl. The fast to total ratio for our sample was measured at 74%, a normal result for this parameter in CsI.

Recognizing that undoped samples have variable properties, presumably due to variation in trace impurities and defects, we are assuming that these differences can be accounted for in the model by variation of a single deep trapping parameter. In the present work, the modeled light yield and proportionality of undoped CsI refer only to the fast (15 ns) component. The slow component of scintillation can be included in this model in future work as the defect(s), their rate constants, and radiative properties become better understood.

IV. MATERIAL PARAMETER TABLES, CALCULATION OF PROPORTIONALITY, AND TIME/SPACE DISTRIBUTIONS

In this section, we detail the application of the model of Sec. II to calculate the proportionality for comparison to the experimental data as already summarized in Fig. 1. For each of the three conditions of sample doping and temperature being modeled, tables of material parameters are provided. These are mainly the rate constants and transport coefficients in Eqs. (1)–(7). We use the parameter values found directly in the literature when possible, or that can be scaled by quantitative physical arguments from parameters known at a different temperature or in a similar material. This is the case for 21 of the 23 parameters listed in Table I for the well studied case of undoped CsI at room temperature. The two remaining values are undetermined for physical reasons and are thus appropriately treated as fitting parameters: K_{1e}, the electron capture rate on deep defects of undetermined identity and concentration, and the incident electron energy at which normalization is performed, since the usual normalization energy of 662 keV turns out to be outside the electron energy range in which the cylinder track approximation is valid. The best-fit values of these two parameters will be examined later when there are additional data on the traps and better understanding of how multiple clusters of excitation in a line act together. In particular, the effect of spacing of excitation clusters along the track on attracting dispersed electrons to the STH track core will be described in Sec. IV A 2.

A. Undoped CsI at room temperature

1. Material parameters and proportionality

Table I lists the material parameters used in the model prediction of proportionality in undoped CsI at 295 K. The first two parameters listed, the initial Gaussian track radius r_{track}, and the average energy invested per electron-hole pair created by an energetic electron, βE_{gap}, are needed to convert dE/dx to the volume-normalized density of excitation via Eq. (8) in terms of which the rate and transport equations (1)–(7) are written. Both the initial radius and the volume-normalized on-axis excitation density are introduced into the equations via the electron and hole generation terms (Gaussian spatial profiles) G_e and G_h in Eqs. (1) and (2). The initially deposited track radius $r_0 = 3$ nm was first estimated for NaI based on consideration of hole thermalization range by Vasil'ev in Ref. [13], then deduced experimentally by equating the expressions for the observed nonlinear quenching in K-dip and interband laser Z-scan experiments on NaI [9]. The value $r_0 \approx 3$ nm was further supported by a calculation of the initial hole distribution in NaI using the NWEGRIM Monte Carlo code at PNNL [22]. We have assigned the same initial track radius in CsI based on the similarity of the two alkali iodides.

The value of βE_{gap} adopted in Table I is required for consistency with the light yield of the 124 000 photons/MeV ± 12,000 (@ 662 keV) in undoped CsI at 100 K measured by Moszynski *et al.* [26]. The listed $\beta E_{\text{gap}} = 8.9$ eV is calculated based on the lower end of the experimental uncertainty range, 112 000 photons/MeV. The band gap of CsI at $T = 20$ K has been reported as 6.02 eV on the basis of two-photon spectroscopy [43]. From this, we may estimate the

room-temperature band gap of CsI as 5.8 eV [9,44]. The CsI light yield at 100 K thus implies $\beta \approx 1.5$ if the light emission is 100 % efficient and if we use the 5.8 eV band gap. Values of β are around 2.5 in most materials [45] including most scintillators [46], so a value of $\beta \leqslant 1.5$ implied for CsI at 100 K is remarkable. Just to assess the effect of adopting a more conservative estimate of the light yield in CsI at 100 K, we ran the proportionality calculation at 100 K for βE_{gap} values corresponding to both 112 000 photons/MeV (shown in Fig. 1) and 90 000 photons/MeV (not shown). The latter choice raises the low energy end of the proportionality curve about 5% relative to the plotted curve for 112 000 photons/MeV. The effect is not dramatic, and is in line with what will be discussed about the effects of lower excitation density in the track on both nonlinear quenching and on the electric-field collection of dispersed electrons back to the core of self-trapped holes.

The electron mobility in CsI has been measured by Aduev *et al.* [49] using a picosecond electron pulse method. The thermalized conduction electron diffusion coefficient D_e is given in terms of μ_e by the Einstein relation, $D = \mu kT/e$. During the hot-electron phase, which has a duration in CsI of $\tau_{\text{hot}} \approx 4$ ps [10], the diffusion coefficient D_e has an elevated value $D_e(T_e)$ relative to the thermalized electron mobility basically because the hot electrons have higher velocity between scattering events. This is an important factor in the early radial dispersal of the hot electrons. Wang *et al.* calculated the peak of the radial distribution of hot electrons in CsI upon their achieving thermalization, as $r_{\text{hot}}(\text{peak}) \approx$ 50 nm [10]. For simplicity in this model, we have assumed a step-wise time-dependent electron diffusion coefficient such that $D_e(t < \tau_{\text{hot}})$ has a constant value that reproduces the Wang *et al.* result of $r_{\text{hot}}(peak) \approx 50$ nm in the solution of Eq. (1) at the end of $\tau_{\text{hot}} \approx 4$ ps. (Wang *et al.* also stated that the tail of the hot-electron radial distribution in CsI extends as far as 200 nm and the tail of the thermalization times is as long as 7 ps [10].) It will be possible in future versions of this model to use a time-dependent $D_e(T_e(t))$ that tracks electron temperature on the picosecond time scale without making the step-wise assumption. The thermalization time and mean radial range of hot electrons, τ_{hot}, r_{hot}(peak), are imbedded in the code because of their use to specify the elevated electron diffusion coefficient $D_e(t < \tau_{\text{hot}})$. The cooling time, τ_{hot}, is also imbedded to enforce the 4-ps delay of capture of electrons on self-trapped holes, which was directly observed in the picosecond absorption spectroscopy of CsI [8]. In the picosecond measurements, the bimolecular capture rate constant B for exciton formation in CsI was time dependent, remaining zero until after the electron thermalization time $\tau_{\text{hot}} \approx 4$ ps, whereupon it achieved the value of $B(t > \tau_{\text{hot}})$ that is listed in Table I.

The self-trapped hole diffusion coefficient and thus mobility at 295 K are known from the literature on thermally activated hopping of self-trapped holes [34,35]. The nonlinear quenching rate constants K_{2E} and K_3 were measured in undoped CsI at room temperature by laser interband Z-scan experiments [9].

The radiative rate R_{1E} and nonradiative decay rate K_{1E} of self-trapped excitons listed in Table I are the room-temperature values of temperature-dependent functions $R_{1E}(T)$ and $K_{1E}(T)$, where the function $K_{1E}(T)$ is assumed to be a thermally activated path to the ground state. In typical treatments of thermally quenched simple excited states, the radiative rate is independent of temperature and can be identified as the decay rate at low temperature. Nishimura *et al.* [36] have shown that the STE luminescence in CsI comes from on-center (type I) and off-center (type II) lattice configurations that communicate over barriers and finally come into thermal equilibrium as the temperature is raised above 250 K. The total radiative rate of the communicating STE configurations is thus temperature-dependent, which we write $R_{1E}(T)$. The temperature-dependent total light yield is then

$$LY(T) = \frac{R_{1E}(T)}{R_{1E}(T) + K_{1E}(T)}. \tag{9}$$

At temperatures above 250 K when luminescence bands of the two STE configurations are no longer distinguishable from one another, the single temperature-dependent decay time of the 310-nm fast intrinsic luminescence band is given in these terms by

$$\frac{1}{\tau_{\text{obs}}}(T) = R_{1E}(T) + K_{1E}(T). \tag{10}$$

These two equations can be fitted to the data of Nishimura *et al.* [36] as well as Amsler *et al.* [55] and Mikhailik *et al.* [56] to obtain the functions $R_{1E}(T)$ and $K_{1E}(T)$ from 100 K up to 295 K. The following method has been used to obtain the values of R_{1E}(295 K) and K_{1E}(295 K) listed in Table I.

To determine K_{1E}(295 K) from data other than proportionality, the model of Eqs. (1) and (3) is first run with the sole objective of reproducing the total light yield of pure CsI at room temperature, which is 2000 photons/MeV for 662 keV gamma rays as published in the Saint-Gobain CsI data sheet [51]. This is also expressible as a 1.8% photon yield per e-h pair produced (using $\beta E_{\text{gap}} = 8.9$ eV). The fitting uses K_{1E}(295 K) as the variable fitting parameter for that single light-yield data point, but it is not varied for fitting the proportionality curve shape. Then Eq. (9) for the reciprocal of the experimentally measured STE decay time at room temperature, $\tau_{\text{obs}} = 15$ ns [36], can be solved for R_{1E}(295 K).

The rate constants S_{1e}, S_{1h}, and S_{1E} for trapping of electrons, holes, and excitons on thallium are proportional to thallium concentration and so are zero in Table I for undoped CsI.

It was argued in Refs. [52,53] based on generalized oscillator strength and Monte Carlo calculations by Vasil'ev for BaF_2 [54] that the number of excitons created initially by stopping of a high-energy electron should be no more than about 4% of the production of electron-hole pairs in wide-gap solids quite generally. This was approximately confirmed for CsI by picosecond absorption spectroscopy [8], which tracked the initially created ($t < 1$ ps) exciton and free-carrier spectra throughout the infrared and visible ranges from 0.45 eV photon energy upward, including the Type I STE peak. The spectra also revealed that the initially created STE population is destroyed within about 2 ps by impact ionization from the hot electrons. Creating hotter initial electrons by exciting 3 eV above the band gap resulted in more complete destruction of the initial STE population [57]. Reconstitution of STEs from bimolecular recombination of thermalized electrons and self-trapped holes did not commence until after a 4 ps delay

for thermalization [8,57]. This is the meaning of our notation $4\%G_e \rightarrow 0$ in the "published" column for the parameter $G_E(r = 0)$. The value used in the model is $G_E = 0$, i.e., the excitons that exist beyond the first 4 ps are those formed later through the bimolecular recombination term Bn_en_h.

The last two rate constants listed govern the capture rates for electrons and holes on deep defects, $K_{1e}n_e$ and $K_{1h}n_h$. The suspected most numerous deep electron traps in pure CsI are iodine vacancies, either empty vacancies as F^+ centers or having trapped an electron to form F centers. We can roughly estimate relative magnitudes of the rate constants K_{1e} and K_{1h} by reference to the equation that relates trapping rate constant K to cross section σ,

$$K = \sigma[\text{trap}]\langle v\rangle, \tag{11}$$

where [trap] is the concentration of the trap and $\langle v\rangle$ is the root mean square velocity of the carriers approaching the trap. The rate constants for capture on otherwise equivalent traps at the same concentrations would scale as the speed of the carrier being trapped. We argue in the following that in alkali halides the contrast between conduction electron and self-trapped hole velocities dominates in comparison to smaller differences in cross sections. The speed of self-trapped holes, calculated as jump rate × jump distance averaged over 90° and 180° jumps, is about 6×10^{-6} of the speed of conduction electrons in CsI at 295 K. The rate constant K_{1h} in Table I is thus listed approximately as $10^{-5}K_{1e}$ if electron and hole traps may be presumed to have similar cross sections and concentrations. Therefore K_{1h} is neglected, leaving only one variable rate constant in Table I, the deep defect trapping rate K_{1e}. The last entry in the table, E_i(norm), is a vertical scaling factor stated as the energy at which the calculated curve is normalized to unity.

The comparison between model and experiment is shown in Fig. 3 below, for undoped CsI at room temperature. The open blue triangles (upper curve) are the experimental Compton-coincidence electron energy response data measured as described in Sec. III. As is the custom, the experimental Compton-coincidence data are normalized to unity at 662 keV. The solid triangular points are the calculated electron response (proportionality) using the parameters of Table I in Eqs. (1)–(7), which reduce to Eqs. (1)–(3) for pure CsI.

2. *Normalization: transition from continuous tracks to separated clusters*

The model is in respectable agreement with the experimental data in the energy range below about 200 keV. In our opinion, the respectable agreement becomes more impressive when one considers that the other curves shown in Fig. 1 were calculated by the same model with parameters that are fairly highly constrained as we will show later in this section. One also notices that with the choice of the normalization energy E_i(norm) for a good fit at energies below 200 keV, the calculated proportionality curve slopes decidedly below the experiment at electron energies greater than 200 keV. In Fig. 1, shown previously, the same is true for CsI (100 K) and CsI:Tl (295 K), where 200 keV is always the normalization energy defining the upper limit of the range for a good fit. A suggestion of what is responsible comes from noticing that the

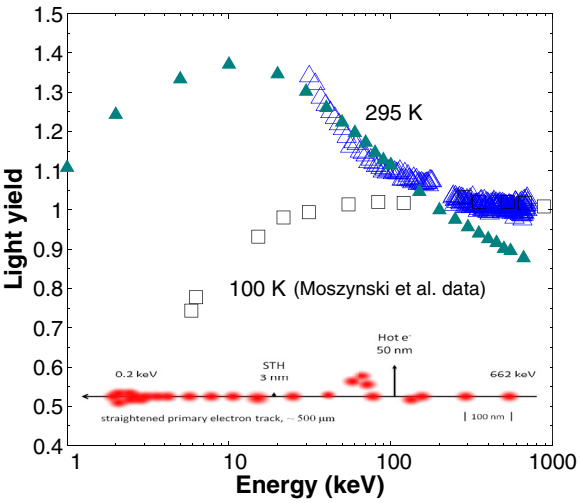

FIG. 3. (Color online) The proportionality curve of electron response modeled by Eqs. (1)–(3) from the material parameters listed in Table I is shown by the solid triangles, and is superimposed on the Compton-coincidence data for undoped CsI (SG sample) at 295 K shown by open triangles. Also shown by open squares is the gamma response experimental curve for undoped CsI at 100 K, to be compared to the model in the next section. The schematic electron track at the bottom (after Vasil'ev [58]), will be used in the discussion.

experimental proportionality curve is nearly flat from 200 to 662 keV and higher for all three CsI data sets and indeed for scintillator materials generally. If all scintillators have proportionality curves nearly flat between 200 keV and the usual 662 keV normalization energy, then we may as well normalize to unity at 200 keV, amounting to a concession that our present model based on a cylinder approximation of the track has a systematic departure from an accurate representation of the experiment above 200 keV. The schematic track representation in the lower part of Fig. 3 illustrates the likely cause. Vasil'ev used a similar track schematic to introduce the concept that energy deposition occurs in a series of e-h clusters at a spacing that increases with particle energy, reaching about 100 nm around 662 keV in NaI [58].

Using a generalized oscillator strength model of the deposition of energy from a high-energy electron, Vasil'ev describes energy transfers during stopping of the electron as producing electron-hole clusters of a size that varies somewhat with the energy of the primary electron but whose mean size is relatively constant in the range of five to six electron-hole pairs per cluster in the high-energy part of the electron track [13,18,58]. Thus, from cluster to cluster, the mean local excitation density within a typical cluster is approximately constant over a considerable range of primary electron energy, and the decreasing energy deposition rate dE/dx with increasing primary electron energy is then mainly reflected as increasing distance between these clusters along the track. When the clusters are far enough apart that each acts in isolation to attract its own dispersed (formerly hot) electrons back to the positive STH cluster core of their origin, the electron response should approach the ideal horizontal line of perfect proportionality. As long as they are far enough apart to be noninteracting, the total light yield of N clusters in a track

segment should just be N times the responses of individual clusters, i.e., proportional. The proportionality curves for most scintillators, including alkali halides on which we are focusing, do tend toward a horizontal line at high enough electron energy.

However, moving toward lower energy of the primary particle and thus higher average dE/dx, the spacing of such clusters along the track becomes smaller [13,58]. One can expect that cooperative effects between the clusters will be manifested. The most important cooperative effect is that of an emerging line charge of STH clusters, as can be appreciated looking at the track schematic in Fig. 3. The 50-nm mean radius of dispersed hot electrons is illustrated quantitatively by the length of an arrow that may be compared to the 3-nm radius of the STH distribution around the track, and to the $\sim$100 nm spacing between clusters typical of 662 keV electron energy in NaI and CsI. Consider a test charge at 50 nm from a line of positive charges (STH clusters). If there are multiple positive point charges along a line segment of roughly 50-nm length, they will all contribute significant radial components to the force on the test charge. The positive charges (e.g., STH clusters) are then acting cooperatively like a line charge segment. In classical electrostatics, the familiar example is the logarithmic (infinite range) potential of an infinite line charge and the extended range even of a finite line charge segment compared to that of a point charge or sphere. Even with screening by an equal number of dispersed electrons balancing the core charge, Gauss's law shows that an enhanced electric field of the line charge extends almost as far as the outer bound of the screening electron distribution.

In the model we have used, significant computational economy was achieved by neglecting clustering and assuming that with each increase in dE/dx there is an increasing but uniform charge distribution that packs into each cylindrical segment of constant radius. This was done knowing that at some elevated energy threshold, separation into clusters will cause the assumption to be inaccurate. What determines that threshold and what is its value? The touching or overlap of clusters has sometimes been regarded as the condition for the track to resemble a cylinder. That is based on a visual concept, but not a physical electrostatic charge-collection criterion. We have calculated the efficiency of electrostatic collection of dispersed electrons in a radial Gaussian (50-nm mean distribution) toward a line containing an equal number of immobile positive charges arrayed in clusters of variable spacing. The result was that as the primary electron energy decreases and forms clusters closer together, the collection efficiency turns upward when the cluster spacing is about 50 nm. From this, we generalize that when the spacing of immobile (e.g., self-trapped) hole clusters in a line becomes closer than the mean radius of dispersed (formerly hot) electrons, they begin to act cooperatively in attracting the thermalized electrons back toward recombination.

The subsequent electrostatic collection after thermalization of distant electrons is essential for forming excitons in the pure material and obtaining radiative emission. As will be further noted in discussing the radial distributions, there is a competition during the electrostatic collection process between the rate of collection back to the central core where the holes are located and the simultaneous rate of electron capture on deep traps. The rate of electron collection is proportional to the density of holes on the axis (excitation density) and to the electron mobility μ_e while the trapping is proportional to the capture rate constant K_{1e} and the density of electrons. These two competing rates, one leading to luminescence within the scintillation gate width and the other not, determine the slope of the high-energy side of the halide hump. That slope underlies the whole modeled proportionality curve. A worthwhile experimental test could be to introduce concentrations of intentional deep defects and measure proportionality, looking for an effect on the slope.

What the local light yield model is unable to reproduce is the rather sharp concave upward bend from a linear downward slope to a nearly flat high-energy region as electron energy goes above about 200 keV. We conclude that the concave upward bend lies outside the rate and transport model itself. It is the crossover from cooperative electrostatics of multiple STH clusters in a line, to independent STH clusters interacting only with their own electrons dispersed to about 50-nm mean distance.

In Fig. 3, the model using the parameters in Table I produces a reasonable match of the falling experimental electron response from 28 keV to about 200 keV. Together with the decrease of yield at even lower electron energy due principally to second-order nonlinear quenching, the model displays the halide hump that is familiar from CsI:Tl electron response. Because of the low light yield of undoped CsI at room temperature, the experimental data end before going over the top of the hump, so that all we see and have available to fit is the slope on its high-energy side.

3. *Population distributions and the luminescence mechanism*

To understand what controls the slope of the proportionality plot below 200 keV, it is helpful to examine how the carriers move and interact with themselves and with traps from the first picoseconds onward. The dependence of the light emission process on the excitation density is believed to be the root of the intrinsic nonproportionality of the scintillator response, so observing the locations and trapping or recombination status of carriers and excitons at low and high excitation density can be instructive. In Fig. 4, we plot the conduction electron density n_e, the self-trapped hole density n_h, the self-trapped exciton density N, and the accumulated density n_{ed} of electrons trapped on the assumed deep defect. The time after excitation for each plot is labeled near the curve. The plotted quantity in all of these radial distributions is the product of radius r and the carrier density, such as $rn_e(r)$, to take account of integrating azimuthally around the track. The gradient along the length of the track is so small relative to the radial gradient that we can assume no net diffusion along the length of the track. Thus the integral over radius and azimuth, or area under these radial plots, should be constant as long as there is no loss from the population such as by exciton formation, trapping, or Auger recombination. The vertical scale units for $rn(r)$ are expressed in mixed form (units of 10^{16} nm/cm^3) on all of the radial distribution plots so that division of the plotted $rn(r)$ value by the radius in nanometers gives the carrier density (cm^{-3}) at that radius.

Figure 4 plots four paired figures showing various radial distributions around the track center for selected times after

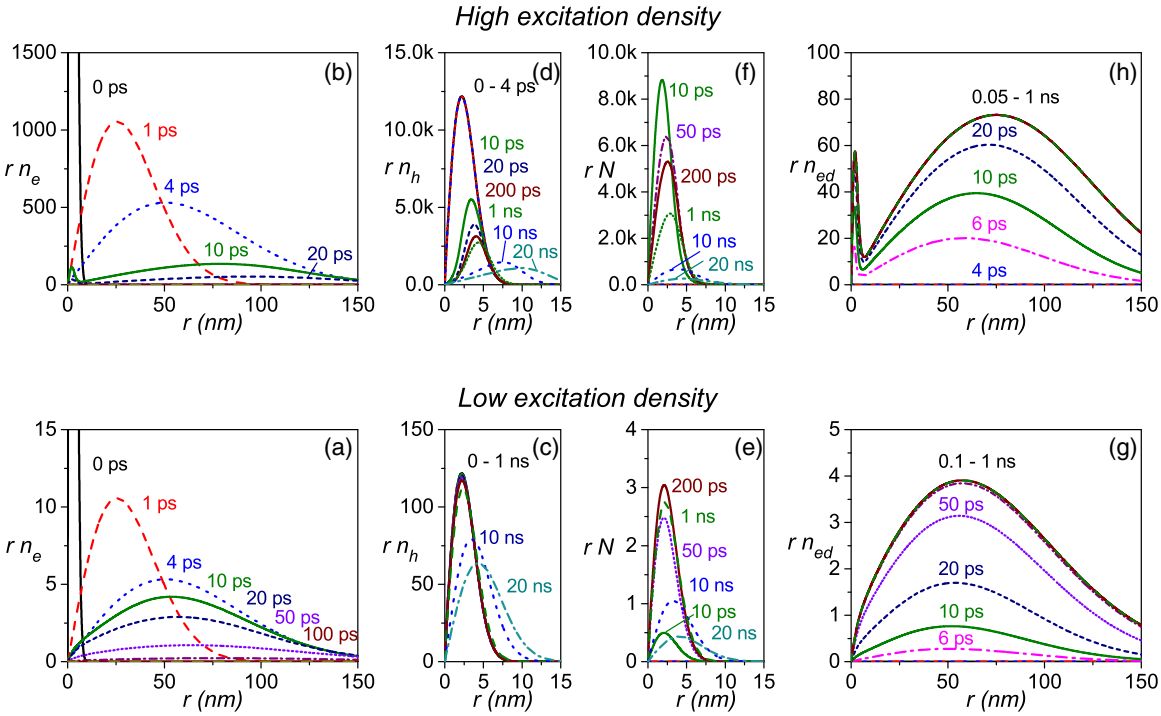

FIG. 4. (Color online) Undoped CsI at 295 K. Radial density distributions for low on-axis excitation density, 10^{18} e-h/cm^3 (lower frames), and 100 times higher on-axis excitation density of 10^{20} e-h/cm^3 (upper frames). Plotted are the azimuthally integrated densities of conduction electrons $rn_e(r,t)$, self-trapped holes, $rn_h(r,t)$, self-trapped excitons, $rN(r,t)$, and the accumulated electrons trapped as deep defects, rn_{ed}. The time after excitation for each plot is labeled on the frame near the curve. The vertical scales are in units of 10^{16} nm/cm^3.

excitation. The material is undoped CsI at 295 K modeled with the material parameters of Table I. In each vertically arrayed pair of figures, the lower figure is for on-axis excitation density of 10^{18} e-h/cm^3, a low value that is encountered in the cylinder track approximation at the beginning of a high-energy electron track, e.g., 662 keV. The upper figure compares the same selection of radial plot times for 100 times higher on-axis excitation density of 10^{20} e-h/cm^3, as encountered toward the end of an electron track where the electron energy is below about 1 keV. Notice that the vertical scale of azimuthally integrated carrier density [e.g., $rn_e(r,t)$ and rn_h] is generally 100 times larger at 100 times the excitation density. Exceptions are made when the plotted species show a big nonlinearity versus excitation density, such as the excitons, rN, and defect trapped electrons, rn_{ed}.

In Fig. 4, frames (a) and (b), we can see the spatial distribution of hot conduction electrons expanding rapidly from creation in a 3-nm track at $t = 0$ ps, past 25-nm mean radius in about 1 ps, and on to the thermalized electron distribution at 4 ps in agreement with the Monte Carlo simulation results of Wang *et al.* [10]. It is worth emphasizing at this point the pronounced outward and subsequent inward migrations of electrons at high excitation density. The outward migration in about 4 ps (in CsI) is driven by excess kinetic energy of the initially formed hot electrons [10]. Its effect, highlighted by comparison of frames (a) and (b) for electrons with frames (c) and (d) for self-trapped holes in Fig. 4, is to separate electrons and holes very rapidly, suppressing exciton formation, free-carrier Auger decay, and second-order quenching at least temporarily. However, as shown in frames (b) and (f) of the figure, the electrostatic attraction of the conduction electrons toward the cylinder (approximately line charge) of positive self-trapped holes asserts itself as the dominant factor at high excitation density after the hot electrons have lost their excess kinetic energy ($D_{\text{hot}} \rightarrow D_{\text{thermalized}}$). Electrons are then drawn back toward the ~3-nm cylinder of STH where they can form self-trapped excitons that ultimately emit light in pure CsI. At low excitation density, on the other hand, deep trapping dominates. The plots in Fig. 4 show that for $n_0 = 10^{18}$ e-h/cm^3 almost 90% of the original electrons are trapped and only about 3% form excitons. We have not explicitly included shallow defect traps, so the electrons that are not captured on the deep defects (rate constant K_{1e}) are regarded as thermalized conduction electrons. This is the same thermalized electron population that is labeled "stopped" in the Monte Carlo simulations of Wang *et al.* [10].

The return migration of dispersed conduction electrons back to the STH core is fast. The peak in exciton formation is reached in 20 ps at high excitation density when about 60% of the original electrons and holes have formed excitons as seen in frames (b) and (f) of Fig. 4. When the on-axis excitation density is high, there is a denser line charge of positive STH in the 3-nm cylinder, thus a larger electric field drawing dispersed electrons radially inward, and so faster collection via the third term in Eq. (1). The time of exposure of those electrons to deep trapping via the $K_{1e}n_e$ term in Eq. (1) is therefore smaller. Accordingly, the total density of deep-trapped electrons (n_{ed}) and the corresponding complement of self-trapped holes left near the core at the end is a strong function of initial excitation density. Along with the nonlinear quenching terms that also

depend sensitively on these radial distributions, *this accounts for the main part of intrinsic nonproportionality* in alkali halide scintillators.

The self-trapped exciton formation via the $Bn_e n_h$ rate term in Eq. (1) is set to zero during the 4-ps hot-electron phase, based on the direct observation by picosecond spectroscopy of STE formation in CsI [8]. According to those experiments, electrons do not begin to be captured on self-trapped holes until they have thermalized. A 4-ps step function delay was built into our model using the parameter τ_{hot} (see Sec. II). On the other hand, picosecond absorption spectroscopy showed that electron capture on Tl^+ commences even during the hot electron phase [8]. This too is contained in the model for thallium-doped CsI (Sec. IV C), although a theoretical reason for the different rates of hot electron capture on STH and Tl^+ is not yet in hand. In the absence of picosecond absorption spectroscopy on the deep defect electron capture, we have assumed that it is zero until after electron thermalization similar to the capture on STH. Thus because of the way we have zeroed STE formation and deep defect capture during electron thermalization, the areas under the electron and hole distribution curves in frames (a) and (c) and (b) and (d) of Fig. 4 are constant for the first 4 ps.

Going beyond 4 ps, capture on STH and defects commences and it can be seen in frames (a) and (b) of Fig. 4 that the conduction electron population decreases significantly in 10 to 50 ps depending on the excitation density. The loss of conduction electrons in this model of undoped CsI is due to the capture on STH to form STE and the capture on the deep defects. The capture of conduction electrons on STH, converting them to STE, can be seen directly as the decrease of STH (n_h) population in frames (c,d) of Fig. 4 and as the creation of STE (N) in frames (e) and (f). The comparison of low and high excitation density in frame pairs (a) and (b), (c) and (d), and (e) and (f) of Fig. 4 supports the conclusion that the recombination of electrons and holes to create (self-trapped) excitons in undoped CsI occurs much faster at high excitation density than at low. This has traditionally been attributed to the fact that the $Bn_e n_h$ rate term is quadratic in the excitation density of electron-hole pairs. As excitation density increases, exciton formation should become increasingly favored over the linear rate of trapping on defects as pointed out by Murray and Meyer [59]. However, frames (a) and (b) and (c) and (d) of Fig. 4 show that the electrons are separated spatially from the self-trapped holes in less than a picosecond during hot electron diffusion, before exciton formation can occur. So there is more to it than just the bimolecular rate term in a uniform distribution of electrons and holes. The term that acts to restore overlap of electron and self-trapped hole populations in undoped CsI is the current of thermalized conduction electrons drawn back toward the positive STH track core by the long-range electric field of this approximate line charge of positive holes. The line charge is screened by the widely dispersed electrons, but they lie mostly outside the STH core so that there is a very strong electric field experienced by the electrons lying close to the core, diminishing farther out as screening charge builds radially. One can see this effect in Fig. 4(b), where the distribution of conduction electrons at 10 ps has its most probable radius shifted out from the 50-nm radius of thermalization at 4 ps to about 80 nm at 10 ps. In the 6 ps after thermalization, more than half of the dispersed conduction electrons are drawn back to the STH core by its electric field, and those come predominantly from the ~50-nm range nearest the core where the screening of the STH core is small. The electrons withdrawn to the track make the remaining electron population asymmetric with a maximum near 80 nm and a lower population toward the track.

In Sec. II, describing the rate equations, we commented qualitatively that if exciton formation occurs at a higher rate for higher excitation density, then competing nonradiative rate terms in the equations such as trapping on deep defects will have less time of exposure to the available conduction electrons and so the radiative yield can be expected to rise. If so, we should see the fraction of conduction electrons captured on deep traps decrease as excitation density rises. Frames (g) and (h) of Fig. 4 plotting the accumulated distribution of electrons on deep traps show this effect clearly. The fraction of created electrons that are cumulatively captured on the deep traps is approximately 5 times smaller for on-axis excitation density of 10^{20} e-h/cm^3 than for 10^{18} e-h/cm^3. This is a strong expression of rising light yield as excitation density increases. At the same time the competing nonlinear quenching term of dipole-dipole transfer will be quadratically stronger with increasing excitation density.

Commenting further on the trapped electron distribution in frames (g) and (h) of Fig. 4, we see that the radial distribution of trapped electrons for high excitation density is asymmetric with a maximum near 80 nm and a lower population toward the track, similar to the skewed conduction electron distribution and for the same reason. A peak of defect-trapped electrons actually appears in the central track core for high excitation density because the many electrons drawn there and awaiting capture by STH are also subject to capture by defects in that region.

The distribution of self-trapped holes in frames (c) and (d) of Fig. 4 deserves a comment on the effect of excitation density as well. We have already noted that the STH population decreases quickly at high excitation density because their cumulative electric field pulls back dispersed electrons which recombine with the STHs to form STEs. However, because some electrons are trapped on deep defects in undoped CsI, there will be a corresponding residual population of STH that do not convert to STE. We can see those in the populations remaining at 10 and 20 ns in frames (c) and (d). The radial diffusion of self-trapped holes is significantly enhanced at the higher excitation density. Because the hot electrons disperse quickly to much larger average radius than the self-trapped holes, there is a repulsive electric field pushing the positive STH apart, and the effect can be seen in frame (d). This becomes an important factor in the nonproportionality of CsI:Tl treated in Sec. IV C. The STH diffuse outward and recombine on a nanosecond scale with the electrons that were captured on thallium as Tl^0 in the first picoseconds in that material. In the presently discussed case of undoped CsI, a similar process may occur as the STH diffuse outward through the field of electrons trapped on defects. If that is the source of the 425-nm defect luminescence in undoped CsI, its lifetime and yield should be related to STH diffusion.

B. Undoped CsI at 100 K

1. Material parameters and proportionality

Table II presents the parameter values used in the calculation that will be compared to experimental proportionality and light yield data for undoped CsI at 100 K measured by Moszynski *et al.* [26]. The low-temperature electron mobility in CsI is scaled from the room-temperature mobility of Aduev *et al.* [49] using the formulas of Ahrenkiel and Brown for temperature-dependent mobility in KBr and KI [60]. In the noncryogenic temperature regime where phonon scattering dominates, Ref. [60] showed that the temperature dependence of their measured Hall mobility fits an exponential expression where the semi-log slope parameter is proportional to the Debye temperature. Using Debye temperatures for CsI, KI, and KBr along with the Aduev [49] room-temperature mobility of CsI to scale from the measured KBr and KI temperature dependencies, we estimate $\mu_e(100\ \mathrm{K}) \approx 31\ \mathrm{cm}^2/\mathrm{Vs}$ in CsI. The thermalized electron diffusion coefficient D_e is then given in terms of μ_e by the Einstein relation.

The diffusion coefficient D_h and mobility μ_h of self-trapped holes in CsI at 100 K are calculated from the thermally activated hopping rate following the references and procedure used for room-temperature values in Refs. [34,35,61]. As remarked in regard to D_E in Table I following Refs. [50,61] the hopping rate of the STE is about the same as for the STH, so $D_E \approx D_h = 1.9 \times 10^{-13}\mathrm{cm}^2/\mathrm{s}$ in Table II.

The STE radiative emission rate constant R_{1E} at 100 K can be read from the temperature dependence of STE decay time plotted by Nishimura *et al.* [36]. Their temperature-dependent luminescence spectra also confirm that the STE emission becomes a nearly pure 3.7-eV band (type II STE) from 100 K down to about 10 K, so R_{1E} at 100 K is the reciprocal of the 900-ns pure type-II STE lifetime. The competing nonradiative STE decay rate K_{1E} must be small compared to R_{1E} because of the plateau in decay time [36] and also the plateau in light yield [36,55,56] that is reached on cooling to 100 K. A detailed look at the Amsler *et al.* plot of temperature-dependent light yield [55] shows that the intensity at 100 K is about 3% below the maximum at 80 K. Temperature-dependent light loss can come from the temperature dependence of defect trapping (see below) and thermal diffusion of STEs to quenching sites as well as thermal quenching of the STE itself (the latter two represented in K_{1E}). If we assume that all of the light loss is from the K_{1E} rate, its upper limit implied by the Amsler data is $K_{1E} \approx 3.4 \times 10^4\ \mathrm{s}^{-1}$ at 100 K. In some sense a more stringent limit is placed by the very large absolute light yield measured at 100 K and its implication (see discussion of Table I above) that β is pushed even lower than 1.53 by any light-loss channel. To accommodate the absolute light yield measurement together with a reasonable β parameter, we have taken the "used" value as $K_{1E} = 0$ in Table II for 100 K. The "published" value based on the Amsler *et al.* [55] data is small as well and makes no noticeable difference in the proportionality curve shape.

The dipole-dipole quenching rate constant K_{2E} describes losses of self-trapped excitons that interact for quite some time at close quarters in CsI at 100 K after electrons thermalize and regather at the line of holes which persists on the track. Because of the resulting importance of dipole-dipole quenching at low temperature, it is prudent to understand if a temperature-dependent trend of K_{2E} can be estimated. The dipole-dipole quenching rate constant K_{2E} depends on the square of the dipole matrix element and the spectral overlap of the emission and absorption line shapes [63]. We do not yet have complete enough data on the temperature-dependent spectra of STE absorption and emission in CsI to calculate the overlap variation, although picosecond absorption spectroscopy toward this goal is underway in our laboratory. The other temperature-dependent factor, the change of the magnitude of the dipole matrix element for emission, can be estimated for CsI from the temperature dependence of the radiative emission rate R_{1E}. The radiative rate constant in simple excited states is usually independent of temperature. However, Nishimura *et al.* [36] have shown that the STE in CsI has communicating populations of on-center and off-center STE [28], that come into thermal equilibrium above 250 K with a single effective lifetime dominated by the fast on-center STE radiative rate. The ratio $R_{1E}(100\ \mathrm{K})/R_{1E}(295\ \mathrm{K}) = 0.164$ is adopted as the approximate scaling factor for $K_{2E}(100\ \mathrm{K})$ relative to $K_{2E}(295\ \mathrm{K})$.

The deep defect trapping rate constant K_{1e} was a fitting variable for the 295 K data, but for the modeling of 100 K data we have scaled $K_{1e}(100\ \mathrm{K})$ from the room-temperature experiment as follows: the best fit of undoped CsI at 295 K yielded the parameter value $K_{1e} \approx 2.7 \times 10^{10}\ \mathrm{s}^{-1}$. There are two reasons that the parameter K_{1e} can be expected to decrease for the modeling of the Moszynski *et al.* [26] sample B at 100 K. One reason is that the sample B seems to have had remarkably low concentration of defects. If we only take into account the 425-nm defect luminescence band in Fig. 2 as an indicator of defect concentration in the SGC sample relative to Moszynski sample B, the SGC sample has about 30% higher defect concentration. The 550-nm band is harder to use for comparison because the photodetectors used in the two studies had different red sensitivity. Based on a comparison of fast to total ratios, we have used an estimated factor of 2.4 more total deep defects in the SGC sample relative to Moszynski sample B (see Appendix C).

In addition, there can be a temperature dependence of the capture rate constant K_1e. The first-principles calculation of carrier capture rate versus temperature by Alkauskas, Yan, and Van de Walle [62] was applied in wide-gap semiconductor systems such as hole capture on the negatively charged center C_N in GaN. In that case, since the capturing center is Coulombically attractive to the carrier, the calculated capture rate attains a minimum value near 100 K and then rises by about a factor 4 as the temperature rises to 295 K. If the defect center is neutral instead, their results for GaN indicated that the temperature dependence is larger, increasing by a factor of approximately 9 from 100 K up to 295 K. Calculations of the temperature-dependent capture rate of electrons on F and F^+ iodine vacancy centers in CsI by the same method, as well as capture on self-trapped holes and on Tl^+ ions in CsI, are in progress [64]. However, since definite results on CsI have not been obtained yet, we have reasoned by analogy to the temperature dependence of carrier capture in GaN that the upper range of expected reduction of K_{1e} on going from SGC undoped CsI (295 K) to Moszynski B undoped CsI (100 K) could be a factor $1/(2.4 \times 9) = 1/21$ allowing for

both sample dependence and temperature dependence. With this scaling factor, we estimate $K_{1e} = 1.3 \times 10^9$ s^{-1} for the electron capture rate on deep defects in Table II for modeling Moszynski sample B at 100 K.

The last two parameters in Table II are assigned the same values used at 295 K. Most such parameters are not listed in Table II, but these two are worthy of comment on why they are left the same. As we have noted, experimental proportionality curves are usually normalized to unity at 662 keV, whereas the energy at which this model is normalized is another parameter, E_i(norm). If, indeed, E_i(norm) marks the approximate transition from independent STH clusters to cooperative STH clusters attracting electrons from their far-flung locations reached at the end of thermalization, it should not change much with temperature or doping since the spacing of energy deposition clusters should not be strongly dependent on either of those variables. To test this hypothesis, we set E_i(norm) fixed at the same 200 keV value already determined by fitting undoped CsI at 295 K.

Theoretically, the Auger rate constant K_3 is also temperature dependent, generally decreasing at low temperature along with the occupation of phonons that can participate in indirect Auger transitions [33]. Considering the comparison of direct and phonon-assisted Auger rates in the work of McAllister *et al.* [33] on NaI, and basing relative populations of zone-boundary phonons at 100 and 295 K on a Debye temperature model similar to that used in Ref. [60], we estimate from the direct/indirect ratio of Ref. [33] that the Auger rate constant in NaI would decrease by a factor 4 at most on changing the temperature from 295 to 100 K. As can be seen in the radial distribution plots, the present transport model shows that the spatial separation of hot free electrons from self-trapped holes is so rapid ($<$1 ps) that the practical importance of free-carrier Auger recombination is very limited. To avoid unnecessary complexity in this early testing of temperature dependence in the model, and recognizing that there remains at present an order-of-magnitude disagreement between theoretical [33] and experimental [9] values of the Auger rate constant in NaI, we have not attempted to predict the change of K_3 with temperature. In Table II, we assign it the room-temperature value measured in Ref. [9].

Figure 5 compares the calculated proportionality curve (electron response) at 100 K, shown by solid square points, overlaid on the experimental gamma yield spectra of proportionality in undoped high-purity CsI (sample B) at 100 K measured by Moszynski *et al.* [26] (open squares).

We can see that the model has shifted from an approximate match of the upward trending data at 295 K to a surprisingly good match with the downward trending data at 100 K in the applicability range below 200 keV. All material parameters were either scaled by physical arguments for temperature and the sample defect content relative to the 295 K experiment and model, or were kept at the 295 K values in a hypothesis that some parameters do not have a big impact by their temperature dependence. The fit appears too good in the sense that perfect overlap of calculated electron response and measured gamma response is not expected. It is generally found that gamma response proportionality curves resemble the shape of corresponding electron response curves for a given material and conditions, but the gamma response curve

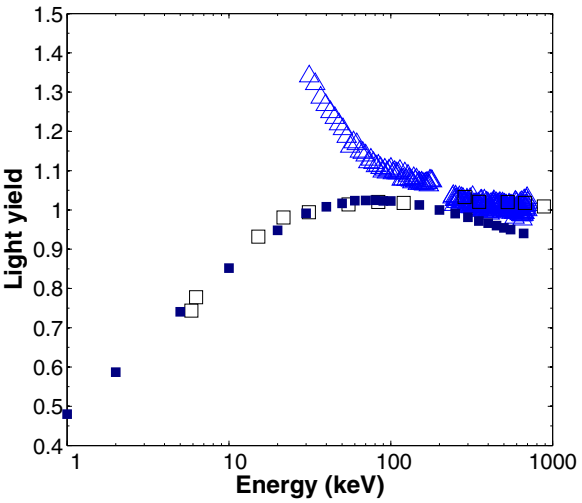

FIG. 5. (Color online) The solid square points show the calculated proportionality curve (electron response) at 100 K using the low-temperature parameters of Table II along with the balance of the parameters kept unchanged from Table I as discussed in the text. The model curve is overlaid on the experimental gamma yield spectra (open squares) of proportionality in undoped high-purity CsI (sample B) at 100 K measured by Moszynski *et al.* [26]. The data of Fig. 3 for undoped CsI(SG) at room temperature are shown as open triangles for comparison.

appears as if shifted to higher energy on the horizontal scale of (logarithmic) energy (see Appendix B).

The experimental data in Fig. 5 make a nearly horizontal line above about 60 keV. The model actually introduces a downward slope beginning above about 100 keV and falling distinctly below the data above the 200 keV normalization point. As noted previously, we believe that this is an artifact from applying the cylinder approximation in the model at energies above 200 keV where the discontinuous deposits of excitation clusters begin to act independently of one another in regard to long-range collection of electrons back toward self-trapped holes.

2. *Population distributions and the luminescence mechanism*

Using the same format established in the previous section, Fig. 6 plots radial distributions at specified times for paired low and high excitation densities of 10^{18} e-h/cm^3 and 10^{20} e-h/cm^3 on-axis for modeled undoped CsI at 100 K with the material parameters of Table II.

The high-density frame (b) for electrons in Fig. 6 at 100 K looks much like the corresponding high-density frame (b) of Fig. 4 at 295 K. The 10-ps curve for conduction electron distribution is about a factor of two lower at 100 K and the small peak of conduction electrons overlapping the STH core at 3 nm is about a factor of two higher at 100 K, all suggesting qualitatively that there is faster collection of conduction electrons in the field of the STH due to the higher electron mobility at low temperature. The conduction electron population decreases due both to capture on STH and capture on defects. Compare frames (g) and (h) of the two figures showing cumulative distribution of electrons trapped on defects at 100 K with those at 295 K. A dramatically

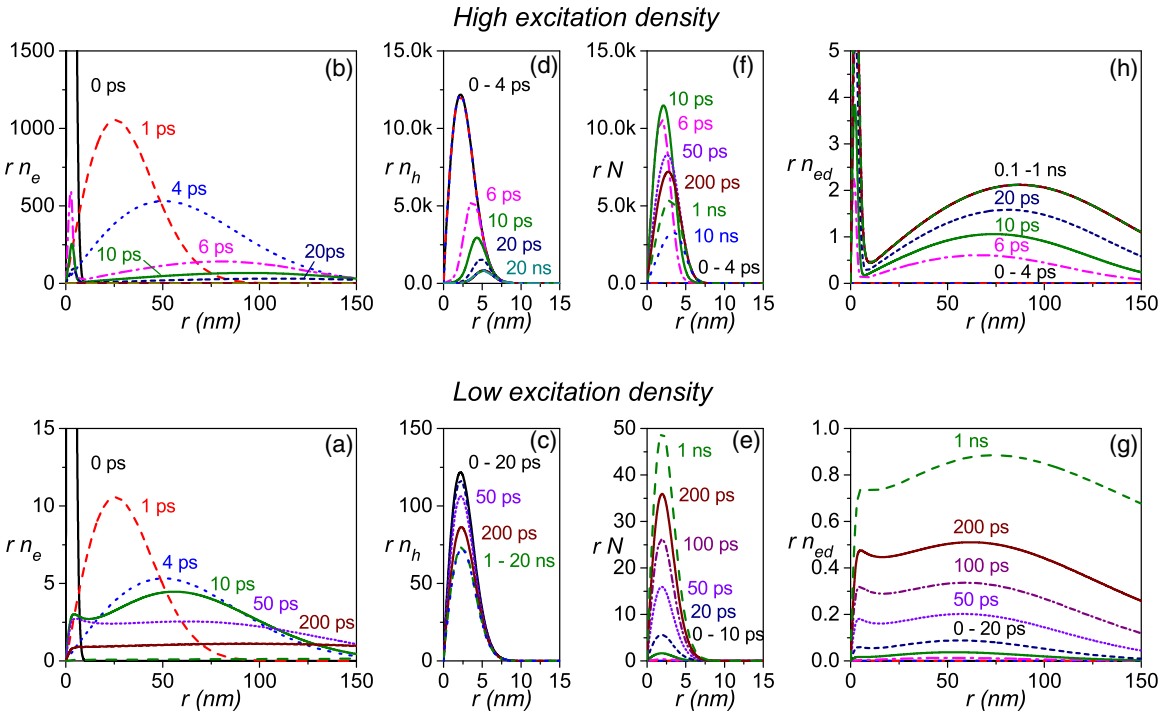

FIG. 6. (Color online) Undoped CsI at 100 K. Radial density distributions for low on-axis excitation density, 10^{18} e-h/cm^3 (lower frames), and 100 times higher on-axis excitation density of 10^{20} e-h/cm^3 (upper frames). Plotted are the azimuthally integrated densities of conduction electrons $rn_e(r,t)$, self-trapped holes, $rn_h(r,t)$, self-trapped excitons, $rN(r,t)$, and the accumulated electrons trapped as deep defects, rn_{ed}. The time after excitation for each plot is labeled on the frame near the curve. The vertical scales are in units of 10^{16} nm/cm^3

smaller fraction of electrons is captured on deep defects at low temperature for high density. [Notice that the vertical scales of (g) and (h) in Fig. 6 are in a much different ratio than the factor of 100 that should be expected if defect trapping were simply proportional to e-h excitation. The azimuthally integrated distributions of defect-trapped electrons are seen to be small fractions of the e-h distributions at 100 K. The reason for less defect trapping is shared by the higher mobility of electrons and the lower cross sections of defects as discussed in connection with Table II.] At low excitation density, the light yield is correspondingly enhanced at 100 K by this effect in addition to less thermal quenching of the STE. The rate equations express competitions between various terms, and faster rates dominate the yield.

Figure 6(a) for low density excitation at 100 K does not appear even qualitatively similar to the corresponding frame of Fig. 4 at 295 K after about 10 ps. With fewer positive STH on axis to pull in the dispersed electrons, the electrons have more time to diffuse in an electric field of the STH core that is evidently of marginal importance in influencing the direction of diffusion. Because of the higher diffusion coefficient at 100 K, a substantial number of the electrons simply escape to larger radius as shown in Fig. 6(a), and become trapped there as seen in frame (g). Noting the vertical scale factors, comparison of the number of trapped electrons in frames (g) of Figs. 6 and 4 shows that even at low excitation density the success of exciton formation versus trapping on defects is improved at 100 K relative to 295 K in undoped CsI.

Comparison of frames (c) and (d) of Figs. 6 and 4 for self-trapped holes at the two temperatures shows as expected that STH diffusion and the electric field enhancement of it at high excitation density are both negligible at 100 K. Comparison of the 10-ps curves at low and high density in Figs. 6(e) and 6(f) confirms visually that the STH convert more rapidly to STE at high density than at low by drawing in the dispersed electrons more quickly and then having a higher bimolecular rate of electron-hole recombination. Conversely, it is the lower rate of this electron attraction and conversion to STE at low excitation density which allowed the diffusion of thermalized electrons to large radius in Fig. 6(a). At high excitation density in frame (f), the STE population has reached its maximum at 10 ps and thereafter begins to decay. This enhanced decay rate at high density may be attributed mainly to dipole-dipole quenching in the 10–100 ps time range. As the figure shows, the reconstructed STE are tightly confined to the initial track radius because that is where the STH reside, and their diffusion is very slow at 100 K. Even though the hot electrons were dispersed to large radius initially, upon thermalization they return very quickly (10 ps) to reconstruct the original track as shown. Despite wide dispersal of the hot electrons, the STE finally form at the STH which retain the memory of the initial track. The high density of excitons in this quickly reconstructed track leads to enhanced dipole-dipole quenching at low temperature, which one can see in the experimental data and in the modeled proportionality. The enhancement of the amount of dipole-dipole quenching relative to what should be expected at higher temperature has at least two origins. The electrons at low temperature survive against trapping better and so create a higher density of STEs when captured in the track core, and the STEs live longer at low temperature and so experience more nonlinear quenching.

TABLE III. Additional rate constants and transport properties used in Eqs. (4)–(6) when modeling CsI:Tl at 295 K.

Parameter	Value	Units	Publ/Est	References and Notes
S_{1e}	3.3×10^{11}	s^{-1}	3.3×10^{11}	ps absorption Ref. [8]
S_{1h}	9.9×10^{7}	s^{-1}	2×10^{6}	varied ratio to S_{1e} from Eq. (11)
S_{1E}	9.9×10^{7}	s^{-1}		equated to S_{1h}
R_{1Et}	1.7×10^{6}	s^{-1}	1.7×10^{6}	Tl^{*} lifetime 575 ns from Hamada [65]
U_{et}[Eq. (1a)]	7.1×10^{5}	s^{-1}	7.1×10^{5}	Tl^{0} decay time 1.4μs Gridin [66]
D_{et}/D_e	2.2×10^{-6}		2.2×10^{-6}	scaled by U_{Tl^0}/S_{1e} factor
μ_{et}/μ_e	2.2×10^{-6}		2.2×10^{-6}	scaled by U_{Tl^0}/S_{1e} factor
B_{tt}/B	2.2×10^{-6}		2.2×10^{-6}	scaled by U_{Tl^0}/S_{1e} factor
K_{et}/K_{1e}	2.2×10^{-6}		2.2×10^{-6}	scaled by U_{Tl^0}/S_{1e} factor
K_{1e}	2.7×10^{10}	s^{-1}		same as CsI; note that K_{1e} scales K_{1et}
B_{et}	2.5×10^{-7}	cm^3/s		assumed same as B
B_{ht}	2.5×10^{-7}	cm^3/s		assumed same as B
K_{2Et}	1.4×10^{-14}	$t^{-1/2}cm^3s^{-1/2}$	1.7×10^{-15}	variable, Z scan in CsI:Tl, Ref. [9]

C. Thallium-doped CsI at room temperature

1. Material parameters and proportionality

Table III displays the additional rate constants and transport parameters used in Eqs. (4)–(6) for trapped electrons, trapped holes, and trapped excitons in predicting the proportionality (electron response) of CsI:Tl (0.082 mole%) at room temperature. All of the parameters used in Eqs. (1)–(3) retain their host parameter values shown in Table I for the pure CsI host when the model is applied to CsI:Tl. K_{1e} is the exception because the defect concentratons can change upon doping.

The first three rates in Table III are the S_{1x}-type energy storage rate constants for electron, hole, and exciton capture on Tl^{+} at the measured concentration of 0.082 mole%. The electron capture rate S_{1e} is the value measured by picosecond absorption spectroscopy in CsI:Tl at 0.07 mole% (0.3 wt% in melt) [8]. According to those experiments, electron capture on Tl starts from time zero and proceeds while the electrons are hot, in contrast to electron capture on STH, which was shown to exhibit a 4 ps delay of onset when the electron energy started 3 eV above the conduction band minimum.

The capture rate S_{1h} of self-trapped holes on Tl^{+} to form Tl^{++} was scaled from S_{1e} by the velocity ratio implied in Eq. (11) relating capture cross section and carrier velocity to the capture rate constant. In this case of electron and hole capture on Tl^{+}, the concentration of the trap is exactly the same in both cases. The capture cross sections were hypothesized to be of the same order of magnitude or closer for electrons and holes since Tl^{+} is a lattice-neutral trap for both carriers. Following the earlier discussion of K_{1e} and K_{1h}, the relevant thermal velocities for S_{1h} and S_{1e} are those of self-trapped holes and conduction electrons, respectively, which are in the ratio of about 6×10^{-6} at room temperature in CsI. Thus the estimated value is $S_{1h} = 2 \times 10^{6}$ s^{-1} by scaling from S_{1e}. The value for best fit of proportionality data was $S_{1h} = 9.9 \times 10^{7}$ s^{-1}.

We have chosen S_{1E} (capture of a self-trapped exciton at a Tl^{+} activator) equal to S_{1h} for capture of a self-trapped hole on Tl^{+}. The thermal velocities estimated from jump rate times average jump length for STH and STE in alkali iodides are about the same [50,61]. The parameter S_{1E} has little effect in fitting proportionality because the population of STEs free of thallium is very small in Tl-doped CsI, mainly due to the enormous trapping rate S_{1e} of electrons on thallium as measured in ps absorption experiments.

Continuing in Table III, the radiative rate of an STE trapped on Tl^{+}, R_{1Et}, is the reciprocal of the published T^{+*} lifetime measured in CsI by direct uv excitation of Tl [65]. The next four parameters in the table are the effective values for electron diffusion coefficient, electron mobility, bimolecular recombination of electrons from Tl^{0} with holes trapped as Tl^{++} and deep defect trapping of electrons while untrapped from Tl^{0}. As discussed in Sec. II, the reason for using these effective time-averaged transport and capture coefficients to represent the trapped electrons on Tl^{0} is to avoid the computational expense of handling short time steps for free electrons simultaneously with long time steps for trapped electrons. The trapped-electron coefficients subscripted with "t" are set as a ratio to the free-electron value of the corresponding parameter: $D_{et}/D_e, \mu_{et}/\mu_e, B_{tt}/B_t, K_{1et}/K_{1e}$. All of the ratios have the same value, because all four of the listed parameters with subscript t refer to time averaged transport or capture of trapped electrons that are inactive and immobile during most of their existence and can diffuse, move in electric fields, or be captured on a different site only during the short fraction of time that the carrier is thermally freed to the conduction band. By this reasoning, the four parameter ratios in the second grouping in Table III are described by just one parameter, which is the ratio of free to trapped electron lifetime in CsI:Tl (0.082 mole%), calculated as follows.

The value for $U_{et} = 7.1 \times 10^{5}$ s^{-1} in Table III is the reciprocal of the Tl^{0} lifetime at room temperature, 1.4×10^{-6} s, as given in the thesis of S. Gridin [66]. Gridin also measured thermoluminescence data and deduced the activation energy for electron release from Tl^{0} in CsI:Tl as $E_A = 0.28$ eV and the attempt frequency as $s = 3.3 \times 10^{10}$ s^{-1} [66]. These parameters yield a room-temperature untrapping rate $U_{et} = 4.5 \times 10^{5}$ s^{-1}. The rate constant U_{et} does not appear directly in the rate equations for reasons discussed in Sec. II, but the ratio U_{et}/K_{1e} determines the fraction of time that an electron trapped as Tl^{0} spends in the conduction band.

The last four parameters in Table III include the capture rate of conduction electrons on deep defects, K_{1e}. K_{1e} in Table I was determined by fitting proportionality in undoped

CsI and is kept at this value in Table III. Next, within the last four parameters, the second-order rate constants for recombination of thallium-trapped carriers with the partner untrapped carrier (B_{et} and B_{ht}) were assumed to have the same values as for the corresponding rate constants of free carriers and excitons. Dipole-dipole quenching of STEs involved in energy transfer and of thallium-trapped STEs in CsI:Tl are together described by the second-order quenching rate constant K_{2Et} which has been measured by laser interband Z-scan experiments [9].

In summary, the parameters in Table III that were allowed to vary for best fit are S_{1h} and K_{2Et}. The values of E_i(norm) and K_{1e} for the host crystal in Table I remain the same as pure CsI. In this sense there are two fitting parameters for CsI:Tl.

We have treated S_{1h} as a fitting parameter, even though its expected value was estimated based on the discussion of Eq. (11), as listed in the "publ/est" column of Table III. The reason for allowing it to vary was that we were unable to obtain a good fit with the estimated S_{1h}, but noticed that a 30 times larger S_{1h} could give a reasonable fit. The other parameters in Table III were held at their estimated values (hence not regarded as fitting parameters), while only S_{1h} and K_{2Et} were allowed to vary near their estimated/measured values, respectively, for good fit. Among the parameters held fixed at estimated values was B_{et}, where the term $B_{et}n_{et}n_h$ is the rate of recombination of STH (n_h) with electrons trapped as Tl^0 (n_{et}). This is one of the two main fates for STH in CsI:Tl, the other being capture on Tl^+ to create Tl^{++} at the rate $S_{1h}n_h$. Capture of free electrons by STH is a main term in undoped CsI, but in CsI:Tl the results in Fig. 10 show it to be a relatively minor third channel because there are very few free electrons in the presence of Tl doping. The summary point is that B_{et} and S_{1h} are the rate constants governing the main two competing channels for capture of STH in CsI:Tl. If one of these rate constants is varied without varying the other, the relative contributions of (STH + Tl^0) and (Tl^0 released electron + Tl^{++}) will be strongly affected. If both are varied together, the relative contributions of these two routes for STH capture and eventual Tl* emission will at least remain in balance.

Against this background, we realized after completion of the work presented here that the estimate given in Table III for B_{et} (only) failed to take Eq. (11) into account and was thus too large. Taking B_{et} too large essentially forced the fitting parameter S_{1h} to assume a value 30× larger than its estimated value, if the balance of STH capture channels discussed just above was to be maintained. An alternative parameter choice that also results in a reasonable fit of the proportionality data is to let B_{et} be the variable fitting parameter rather than S_{1h}, which would in this case be fixed at the value in the "publ/est" column of Table III, not 30 times larger. With offsetting parameters like S1h and Bet, there remains some arbitrariness in choosing which to fix and which to vary. However, there is more information available about this pair of parameters (i.e., their "balance" as noted) than would correspond to just declaring both as free fitting parameters. Resolving the arbitrariness should be helped when the model is required in ongoing work to fit the decay-time components in CsI:Tl, their relative strengths, and total light yield (see also next paragraph). This work is underway, and should become an example of how uncertainties remaining in the current model parameters will be restricted as more kinds of data are fitted, not just proportionality.

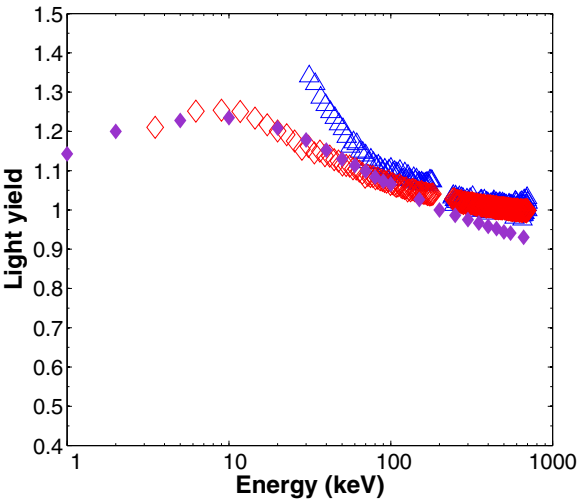

FIG. 7. (Color online) Solid diamonds plot the calculated proportionality curve (electron response) using the combined parameters of Tables I and III for 0.082 mole% thallium-doped CsI at room temperature inserted in the model of Eqs. (1)–(7). The model curve is overlaid on the Compton-coincidence experimental proportionality curve of CsI:Tl (0.082 mole%) at 295 K shown by the open diamonds. The experimental data for undoped CsI (295 K) are reproduced in this figure by open triangles for comparison.

Figure 7 shows with solid diamond points the calculated proportionality curve (electron response) using the combined parameters of Tables I and III in the Eqs. (1)–(7) for 0.082 mole% thallium-doped CsI at room temperature. The model curve is overlaid on the Compton-coincidence experimental proportionality curve of CsI:Tl (0.082 mole%) at 295 K shown by the open diamonds. The data for undoped CsI are reproduced in this figure as open triangles for comparison. The Compton-coincidence measurements for both the CsI and CsI:Tl samples were done in close succession on the same apparatus as described in Sec. III. All the model curves are normalized to unity at 200 keV, for reasons already discussed regarding the validity ranges of the cylinder and cluster track approximations. The room temperature light yield of CsI:Tl at 662 keV is 54 000 ph/MeV from the Saint-Gobain data sheet [51]. The model predicts lower absolute light yield of 26 000 ph/MeV at 662 keV (somewhat too low because of the cylinder approximation breakdown) and about 28 000 ph/MeV at 200 keV.

Comparison of the experimental proportionality curves for undoped and Tl-doped CsI in Fig. 7 supports a general conclusion that Tl doping makes the response more proportional. On the one hand a difference in proportionality should not be surprising given what the model is demonstrating about the quite different recombination paths leading to STE emitters and Tl* emitters in the two systems, but on the other hand, finding that CsI:Tl in fact has the flatter proportionality suggests looking again (e.g., Gwin and Murray [38]) for a Tl concentration at which the proportionality might be optimized,

and for a careful study of modeled proportionality through the transition from "undoped" to doped material. This model could be a tool for understanding detailed effects of activator concentration.

2. *Population distributions and the luminescence mechanism*

Glancing visually at the proportionality data and its model fit in Fig. 7, one might judge that the thallium doping produced a set of physical phenomena and rates about midway between those occurring in undoped CsI at the two temperatures of 295 and 100 K. The hump is about half the size as in undoped CsI at the same temperature of 295 K, so it might be suggested that there is only a moderate change in the physical processes because of one or more things going to half or twice their rates and ranges. However, such an impression is qualitatively wrong! As we shall see while considering the spatial and time profiles of various carriers, capture locations, and recombination events with and without thallium, the route to light emission takes dramatically different paths in undoped and Tl-activated CsI. The marvel really is that the proportionality curves at room temperature end up looking as similar as they do! However, in at least one sense, it seems that there may be a fundamental reason for the similarity of proportionality curves for CsI and CsI:Tl after all. It lies in the existence of a track core of low-mobility self-trapped holes interacting electrostatically with electrons that were widely dispersed during an initial hot-electron phase. In pure CsI, the thermalized electrons are mobile conduction electrons, while in CsI:Tl, they are mostly trapped on Tl^+ to form Tl^0. Many of the same basic interactions including charge separation and then attractive recombination of charge-separated carriers to form light-emitting excitons (free or activator-trapped) go on in the two systems. In CsI:Tl, some of these processes go on at a much slower rate because the carriers are trapped most of the time. This longer time scale allows competing processes to become more significant and means that self-trapped hole diffusion, although slow, can become an important factor.

The radial distribution plots from modeling CsI:Tl at 295 K with the parameters in Table III are shown in Figs. 8–10. The plots that are shown were calculated for the on-axis excitation density of 10^{19} e-h/cm^3, mid-way on a logarithmic scale between the high and low densities compared above for undoped samples. Figure 8(a) displays the azimuthally integrated conduction electron density rn_e. The initial distribution in the 3-nm track is seen going off scale vertically on the left at $t = 0$ ps. The next distribution at $t = 1$ ps catches the hot electrons in outward flight as before. The curve for $t = 4$ ps is peaked near 50 nm as in the undoped samples, but it is already greatly diminished in area because electron trapping on the thallium dopant proceeds with a 3-ps time constant measured in the picosecond absorption experiments discussed earlier [8]. By 10 ps, free conduction electrons are no longer visible on this plot. Figure 8(b) plotting electrons trapped as Tl^0 (rn_e) shows where the electrons are going; they have been immobilized on this short time scale in a distribution of $Tl^0 = n_{et}$ peaking at about 20 nm radius. In contrast, the dispersed electrons in the undoped crystal remained free until they were pulled back to the STH core to form STEs, or were trapped in deep defects. This establishes an important difference between

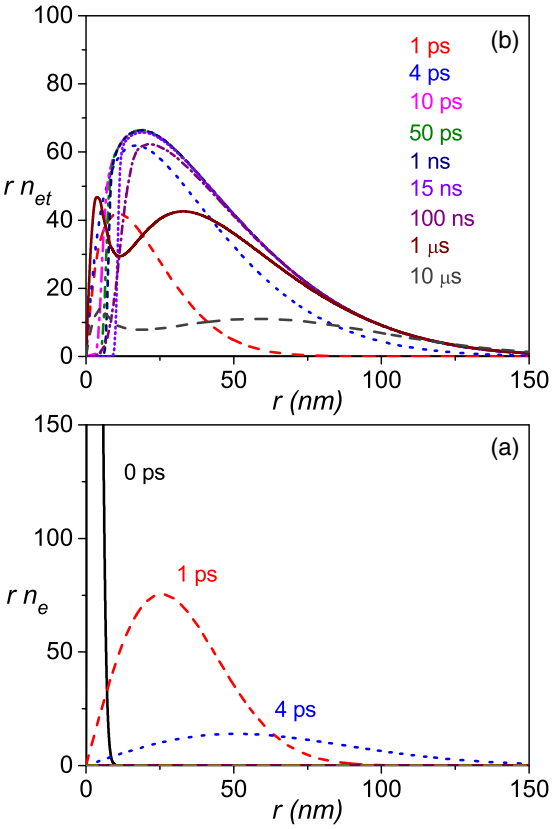

FIG. 8. (Color online) CsI:Tl 295 K. Radial density distributions for (a) the azimuthally integrated conduction electron density $rn_e(r,t)$ and (b) the thallium-trapped electron density $rn_{et}(r,t)$ both for an original on-axis excitation density of 10^{19} e-h/cm^3. Times after the original excitation are shown in the plots. The vertical scales are in units of 10^{16} nm/cm^3

radially dispersed mobile conduction electrons and radially dispersed trapped electrons on the Tl activator as effective starting points for recombination in pure CsI versus CsI:Tl. We have not tried, other than by color online, to associate a time with each curve in Fig. 8(b) because these same data are replotted in Fig. 9 on expanded scales so the labeling can be more clearly applied.

The distribution of electrons trapped by Tl^+ dopant as Tl^0 (density n_{et}) is shown in Fig. 9 with an expanded scale focused on 0 to 25 nm and divided into two time groups, 0 to 15 ns in frame (a) and 15 ns to 10 μs in (b). Theses plots show clearly what was stated in the paragraph above, that the peak of the trapped electron distribution is at 20 nm in contrast to the peak of thermalized electrons at 50 nm in undoped CsI. This expresses what was built into the model on the basis of the picosecond absorption experiments showing that hot electrons are captured on Tl^+, with an exponential trapping time of 3 ps, that is shorter than the conduction electron thermalization time. Thus some of the hot electrons are captured by Tl^+ "in flight" on their way out toward what would have been the 50-nm distance of thermalization. This has the practical consequence of keeping Tl-trapped electrons close to the STH core and thus affecting the probability of recombination by STH diffusion and electron de-trapping from Tl^+ in the plots below.

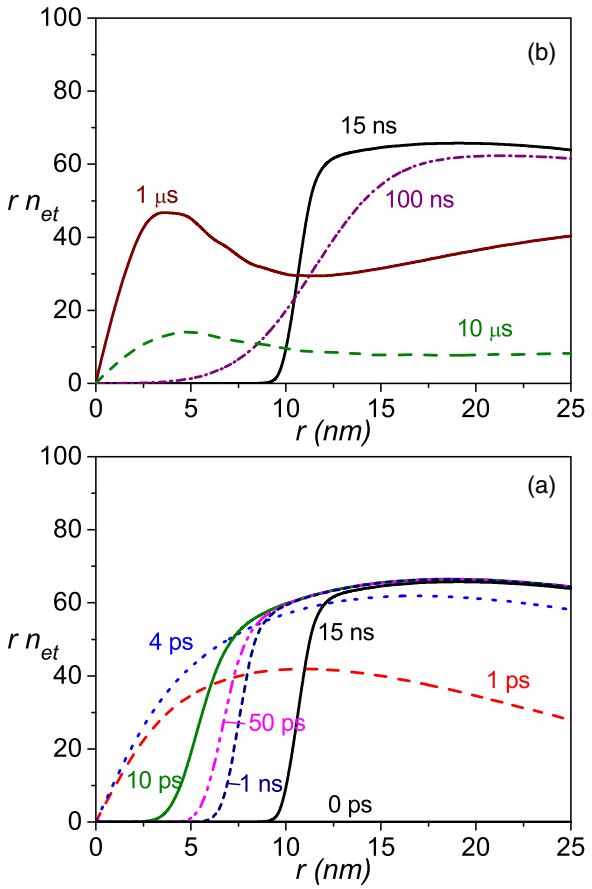

FIG. 9. (Color online) CsI:Tl 295 K. Expanded view of the radial Tl-trapped electron density distributions $rn_{et}(r)$ shown first in Fig. 8 but here shown from 0 to 25 nm with curves divided into two groups, 0 to 15 ns in frame (a) and 15 ns to 10 μs in (b). This is the distribution of electrons trapped by Tl^+ dopant to form Tl^0 The vertical scales are in units of 10^{16} nm/cm^3

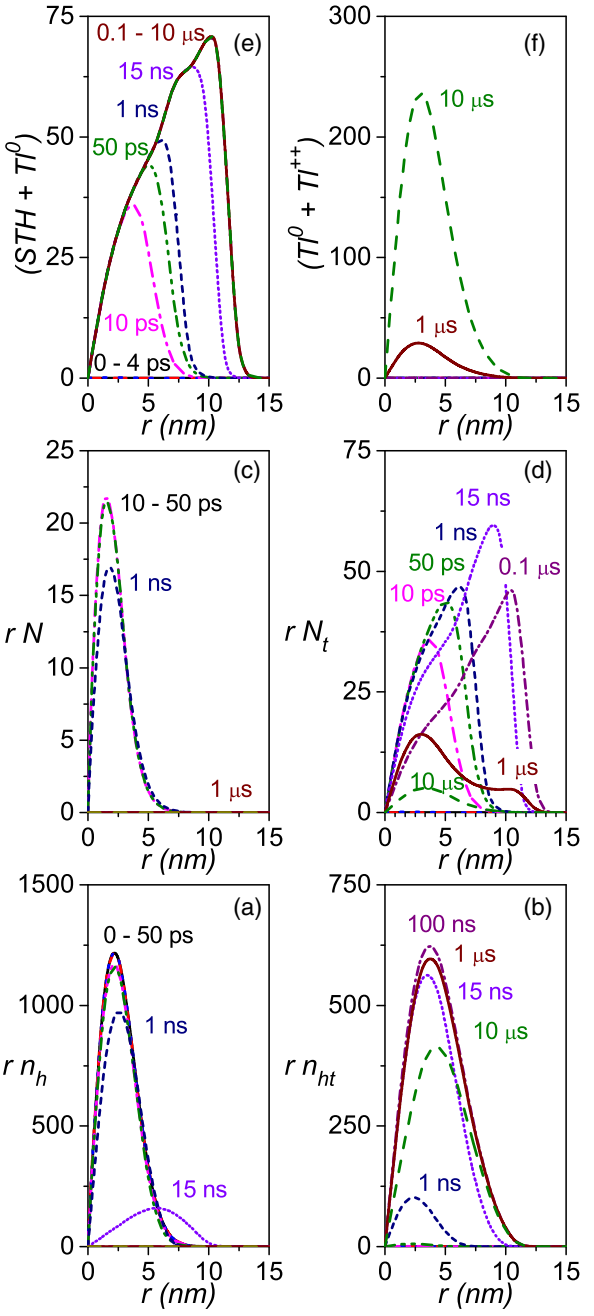

FIG. 10. (Color online) CsI:Tl 295 K. Radial density distributions for (a) rn_h self-trapped holes, (b) rn_{ht} Tl-trapped holes, (c) rN self-trapped excitons, (d) N_t Tl-trapped excitons, (e) STH +Tl^0 self-trapped holes combining with Tl that has already trapped and electron, and (f) Tl^0 + Tl^{++} Tl-trapped holes migrating to combine with Tl^0 all for an original excitation density of 10^{19} e-h/cm^3. The vertical scales are in units of 10^{16} nm/cm^3.

In Fig. 9(a), one can see the captured electron distributions growing at 1 and 4 ps, both starting up from the origin with nonzero slope. Then proceeding forward from 10 ps through 15 ns, one sees a steep initial slope eating into the otherwise stable and extended distribution of trapped electrons (Tl^0). In the central core the STH population (n_{ht}) and the Tl-trapped electrons (n_{et}) intermingle in the same space. In regions where the densities are the highest, trapped electrons and holes are closest to one another, and it takes less time for hole diffusion to create STEs on neighboring trapped electrons. The result is that trapped electrons are eliminated first in the middle and the time to elimination increases as the radius increases. We see this effect as an increase in the point where the trapped electron distribution begins. This transformation eliminates trapped electrons from the center outward through about 1 ns even though the shape of the hole distribution changes little in this time frame.

Figure 10 provides radial plots for additional entities. Comparing the thallium trapped electrons just viewed to the plot of STH (n_h) distribution in Fig. 10(a) confirms that to 1 ns the hole population is essentially stationary but between 1 and 15 ns the hole distribution has expanded radially outward and now this progressing front of holes is consuming trapped electrons and converting them to trapped excitons. At any given time in this range, the tail of the STH radial distribution coincides with the initial rise of the steep slope in the Tl^0 distribution; i.e., the STH are diffusing out and recombining with Tl^0 to create the emitting centers, excited Tl*, represented as trapped density N_t in Fig. 10(d). This is a very graphic

illustration of how STH diffusion controls the rate of creation of excited thallium activator in the nanosecond time range. This rate of creation and the 575-ns lifetime of the Tl* excited state are expected to bring about the rising part of the fast 650-ns emission in CsI:Tl. Within 100 ns, the STH population plotted as rn_h in Fig. 10(a) has decreased to a level indistinguishable from the baseline, consumed both in recombination with Tl^0 and in trapping as Tl^{++} (n_{ht}), shown in Fig. 10(b).

Once the diffusing STH are gone, the curves for times of 100 ns and longer take on a different radial profile as seen in Fig. 9(b). The steep edge softens as the distribution of Tl^0 shifts by detrapping of electrons from Tl^0, diffusing back toward the origin, drawn there by attraction of the positive track core of Tl^{++}. It can be seen that the 1 μs curve of Tl-trapped electrons (Tl^0) in Fig. 9 develops a peak near the track core due to this influence, and then decays substantially up to 10 μs as recombination of the untrapped Tl^0 electrons with the Tl^{++} occurs to produce a later stage of Tl* and consequent light. This constitutes the 3-μs decay time component of CsI:Tl. From the 10-μs curve, one can see that the collection of detrapped Tl^0 electrons is accelerated for the close ones, where the electric field of the track core is relatively unscreened, whereas the distant ones represent a growing proportion of the radial distribution of electrons stored as Tl^0. They will contribute to afterglow or simply find defect traps at longer times. Again, this graphically associates different radial portions of the hot dispersed and then trapped electrons with different identified decay time components of the emission in CsI:Tl.

Figure 10(a) shows the distribution of self-trapped holes at density rn_h. The population remains constant out to 4 ps because the model prevents electron capture on STH until after electron thermalization in keeping with picosecond absorption experiments [8]. It then decreases only slowly for the following nanosecond, because there are almost no free electrons for recombination, and the STH must diffuse to find electrons trapped on Tl^0 or to become trapped as Tl^{++}. Only a small number of STH remain at 15 ns and virtually none at 100 ns.

Figure 10(b) shows the evolving distribution of Tl^{++} (density n_{ht}). It grows monotonically up to 100 ns by trapping of STH on Tl^+. From the n_h plot in frame (a) we have just seen that the STH population is exhausted at 100 ns. From that time on, the Tl^{++} population decreases slowly by recombination with electrons released from Tl^0 to produce light emitting Tl*, with about 2/3 of the maximum Tl^{++} population remaining at 10 μs. Those will contribute to afterglow or be caught on deeper defect traps at longer time.

Figure 10(c) shows the distribution of self-trapped excitons not associated with activators. The main comment here is that they are confined to about 4-nm radius and that the STE population is roughly three times smaller than that of Tl*. This does not mean that STE emission will be 0.3 times the intensity of Tl* emission, because the STE population is subject to strong thermal quenching. With quenching taken into account, this STE population will hardly produce any observable luminescence at room temperature, in agreement with observation.

Figure 10(d) shows the evolution in time of the distribution of excitons trapped on thallium, or simply excited Tl* (density rN_t). This is the state mainly responsible for emission of light in CsI:Tl and can be formed by recombination of STH with Tl^0, capture of STE on Tl^+, or capture of an electron (free or released from Tl^0) on T^{++}. We see the earliest distribution of Tl* at 10 ps as a nearly symmetric peak versus radius. This 10-ps distribution qualifies as "prompt" creation of Tl*. Going forward in time to 50 ps and 1 ns, the peak becomes asymmetric as the frontier of STH + Tl^0 recombinations moves outward. This is the beginning of the observable slow rise of the fast 650-ns component of Tl* emission in CsI:Tl. At 15 and 100 ns, the addition of Tl* population at the frontier of diffusing STH continues, but radiative decay of the whole population has also started (with 575-ns lifetime [65]). Up to this point the radial distribution of N_t (Tl*) results almost entirely from the recombination of STH with Tl^0 as clearly indicated by the shapes of the curves in Figs. 10(d) and 10(f). Going forward still more to 1 and 10 μs, the frontier stops moving outward because the STH population is exhausted. A peak emerges near the track core as electrons start to be untrapped from Tl^0 on the μs time scale and are drawn in by the positive charge of Tl^{++} [frame (b)] near the track core. The rate of light emission from Tl* is just $R_{1Et}N_t$, where $R_{1Et} = 1/(575\ \text{ns})$ is the radiative decay rate of Tl*. We will discuss sources and losses of the Tl* (N_t) population below. Separating the components in time, it is possible to deduce predictions of proportionality of each of the spatial and decay-time components. This should allow comparison of the model to the decay-time associated proportionality measurements reported by Syntfeld-Kazuch *et al.* [67] in a future publication.

Figures 10(e) and 10(f) plot two time-integrated source terms contributing to the population N_t (Tl*), specifically the third and fourth terms of Eq. (6) for the thallium-trapped exciton population N_t. The solution of Eq. (6) as plotted in Fig. 10(d) includes the effects of loss terms for radiative decay and dipole-dipole quenching, but one can readily see qualitative correspondence between the radial distributions in Figs. 10(e) and 10(f) and the several humps in Fig. 10(d) representing identifiable physical processes and their spatial locations contributing to the Tl* excited state that emits light.

As we have mentioned, the plot in Fig. 10(e) can be considered as a source of the fast (650 ns) scintillation in CsI:Tl, while the graphs for 1 and 10 μs in Figs. 10(d) and 10(f) indicate the source of the middle (3 μs) decay time component of scintillation in CsI:Tl at room temperature, probably including components of afterglow. Experiments are available that show for particular doping levels and experimental conditions that the fast component accounts for about 75% of the light and the 3-μs component accounts for about 25% of the light [68,69]. Attempting to reproduce these relative magnitudes of emission taking into account the Tl* formation rates and the decay kinetics will constitute a more rigorous additional test of the model and especially the material parameters that enter it.

The rate of recombination of free conduction electrons with Tl^{++} according to the rate term $B_{ht}n_en_{ht}$ is found to be negligible because the Tl^{++} form slowly [see Fig. 10(b)] and the free electrons do not last very long in the presence of Tl^+. Also, electron trapping on deep defects becomes nearly negligible when thallium is present, because the thallium is

at higher concentration than typical defects and is a very good electron trap. The point is that deep electron traps are so overwhelmed by the efficient and numerous thallium traps in CsI:Tl (0.082%), that they barely become populated on the scintillation time scale of 10 μs. Their effect on proportionality is greatly reduced in CsI:Tl compared to undoped CsI.

V. CONCLUSIONS

From the outset, the system of coupled transport and rate equations that we proposed for analyzing recombination luminescence in electron tracks is plausible and is likely general enough to apply in a wide range of materials used as scintillators if one can express the transport and capture coefficients properly for hot carriers as well as thermalized ones. Criticism could be made regarding omitted rate terms, which we tried to distinguish on the basis of whether they are likely to affect light emission within scintillator gate widths of 10 μs or less. Criticism could also be made of the cylinder track approximation, but the results of the model itself have pointed quantitatively to the range of validity of the cylinder versus independent cluster approximation ($\leqslant$200 keV), along with the related empirical observation that above 200 keV the proportionality of scintillators in general becomes nearly flat at the value associated with 662 keV. At the higher energies, excitation clusters act independently to try to electrostatically recover their own dispersed hot electrons, while at the lower energies they act in concert as a line of positive charges with increasing success as the long-range potential of a line charge becomes better realized by clusters spaced closer than the mean radial range of hot electrons. The interesting (and technologically troublesome) nonproportionality features generally occur below 200 keV, where the cylinder approximation is adequate and provides computational economy along with conceptual clarity in representing the complex interplay of populations in spatial, temporal, and excitation-density coordinates. This study of CsI under different temperature and doping conditions is intended as a first validation test toward the goal of qualifying an agile computational model for studying particle track recombination processes in many materials including dopant, defect, and temperature variations. So why was CsI chosen as the first subject, and what has it shown us?

CsI has a slow electron thermalization time because of its low LO phonon frequency [10]. In common with other alkali halide crystals and in contrast to most oxides and semiconductors, holes in CsI are self-trapped. CsI:Tl gained early application as a bright scintillator along with NaI:Tl, and for many decades up to about the year 2000 it held the record highest light yield among practical scintillators. Undoped CsI is itself a useful fast scintillator, if not a bright one. Empirically, the proportionality curve of CsI:Tl shares with other alkali halide crystals the "halide hump" distinguishing them from almost all other scintillators. This drew us to CsI for testing a model because the hump (actually the slope of light yield forming its high energy flank) offers more of a challenge and distinction between materials than the ubiquitous roll-off of light yield toward low electron energy. Furthermore recent experimental demonstrations that low temperature could eliminate the halide hump [26] and that Tl doping (or not) also influenced it made meaningful testing more likely for what are otherwise fairly structureless experimental proportionality curves. The properties just listed may all be related, but it was not obvious how. One conclusion of this study is that they are indeed related, and the results of modeling show how.

One additional aspect of CsI that led us to choose it for this first study is that many of the needed rate and transport coefficients for CsI have been measured or calculated. Even so, another general conclusion from this work is that with so many rate, transport, and track structure parameters needed in the coupled equations (1)–(7), it is not reasonable to expect that one can for an arbitrary material measure the 20 or more parameters accurately enough to plug in and obtain the proportionality and light yield directly. The very nature of a rate equation model is that it states balanced competitions among various terms. A practical application of the model is likely to be discovering the competitions that have the largest effects on proportionality and light yield, e.g., outward and inward radial electron currents in CsI, and secondary competitions that affect the primaries. Then computational experiments of changing concentration, temperature, co-dopant, and defects can be studied as perturbations on the working model for the material at hand.

Prior to the full model of Eqs. (1)–(7), we had applied a simpler model consisting approximately of Eqs. (1) and (2) for thermalized diffusion to look for general trends versus ambipolar diffusion coefficient in materials including oxides, some semiconductors, and halides [16]. The basic hypothesis of the earlier model was that larger ambipolar diffusion coefficient would alleviate high density in the track core and thus alleviate second- and third-order nonlinear quenching that are considered the main cause of the ubiquitous roll-off of light yield for low electron energies (high excitation density) [2]. For the oxides and semiconductors surveyed, the modeled "avoidance of nonlinear quenching" correlated well with an experimental parameter representing a measure of proportionality [16]. However, the alkali halides including CsI:Tl lay well outside the model trend [16]. It was obvious that something essential about the halides was being neglected. A conclusion from the present study is that hot electron dispersal, resultant separation from the positive charge of relatively immobile self-trapped holes, and collection again of the electrons toward the line charge formed by cooperating STH clusters at linear spacing less than the approximate mean radial distance to the ejected hot electrons (corresponding to energies less than about 200 keV) were being neglected and should not have been. Now the situation turns again. While the earlier simplified model of Eqs. (1) and (2) expressed only for thermalized carriers could fit some trends among different oxide materials (including YAP:Ce as one datum), the recent finding that different samples of YAP:Ce (cerium-doped yttrium aluminum perovskite) have quite different proportionality curves [39] is beyond the finesse of the simple Eqs. (1) and (2). We expect that the full set of Eqs. (1)–(7), or an extended set of 11 equations if another defect or dopant is involved, are general enough to look at such cases in broader categories of materials. Modeling of YAP:Ce for different concentration of Ce is underway. The general conclusion is that we have a testable model which

has already revealed useful insights about the workings of recombination in the electron track environment of CsI for different temperatures and doping, and can now be tried in more general classes of scintillation materials.

ACKNOWLEDGMENTS

WFU and LBNL acknowledge support from the National Nuclear Security Administration (NNSA), Office of Defense Nuclear Nonproliferation Research and Development (DNN R&D) under Contract LB15-V-GammaDetMater-PD2Jf-LBNL AC02-05CH11231. WFU acknowledges support from the US Department of Homeland Security, Domestic Nuclear Detection Office (DNDO), 2014-DN-077-ARI077-02 and the US National Science Foundation (NSF), ECCS-1348361, in a jointly sponsored Academic Research Initiative (ARI). This support does not constitute an express or implied endorsement on the part of the Government. We thank S Kerisit, A. N. Vasil'ev, K. B. Ucer, S. Gridin, K. Biswas, A. Alkauskas, A. Burger, S. Payne, M. Moszynski, L. Swiderski, A. Syntfeld-Kazuch, and A. V. Gektin for helpful discussions and assistance.

APPENDIX A: ORIGIN OF THE 4.1-eV ROOM TEMPERATURE LUMINESCENCE IN PURE CsI

Nishimura *et al.* [36] and Belsky *et al.* [70] published nearly simultaneous experimental studies with interpretive attributions of the 4.1-eV (310-nm) fast intrinsic luminescence of CsI at room temperature. Nishimura *et al.* excited CsI by two-photon absorption of 3.18 eV laser light, and plotted the intrinsic luminescence spectra, lifetime components, and integrated yield of the lifetime and spectral components from 6 K up through 300 K. They could identify known bands and lifetime components of self-trapped excitons at the low temperatures (below $\sim$126 K). Upon further analysis, they attributed the 4.3- and 3.7-eV low-temperature luminescence bands to on-center (type I) and moderately off-center (type II) lattice configurations of the STE. Furthermore, singlet and triplet lifetime components of each STE configuration were identified. Then Nishimura *et al.* presented an analysis consistent with thermal equilibration of the on-center and off-center STE configurations above $\sim$150 K to produce a single main band at the new luminescence energy of 4.1 eV, which persisted up to room temperature and displayed a 15-ns lifetime. The 4.1-eV band energy of the equilibrated populations is close to the 4.3-eV energy of the pure type-I STE because the type-I configuration has the strongest radiative transition rate and represents the dominant radiative channel out of the equilibrated STE population. The integrated intensity of the 4.1-eV luminescence is diminished relative to integrated intensity at lower temperature. In CsI, Nishimura *et al.* attributed the quenching tendency on approaching room temperature to mobility of the STEs when in the on-center configuration, such that they transfer energy to impurity/defect centers including the surface. Specifically, they compared their observation of the 4.1-eV room-temperature luminescence using 6.36 eV excitation by two-photon absorption with the finding of Kubota *et al.* [71] that one-photon ultraviolet excitation in the near-edge fundamental absorption at room temperature does not excite 4.1 eV luminescence, and suggested that STE diffusion to surface quenching centers is responsible. To further support this interpretation, Nishimura *et al.* commented that they were unable to excite the 4.3- and 3.7-eV STE bands with one-photon ultraviolet excitation at temperatures above 160 K. Williams *et al.* [19] were able to excite weak luminescence of CsI in the 4.1-eV range at room temperature with 5.9-eV one-photon excitation by high intensity subpicosecond pulses. The lifetime shortening to 1.4-ns rather than the 15-ns bulk lifetime was attributed to the competing de-excitation route of surface quenching, and the ability to see the one-photon excited STE luminescence at room temperature was attributed to saturation of the surface quenching centers under intense subpicosecond excitation of 10^{18} to 10^{20} electron-hole pairs per cm^3 [19].

The publication of Belsky *et al.* on fast intrinsic CsI luminescence [70] in the year preceding the publication of Nishimura *et al.* [36] was apparently so close in time that it did not receive comment in the Nishimura paper published in the same journal. Belsky *et al.* used tunable synchrotron radiation to measure excitation spectra of the 4.1-eV luminescence in CsI at room temperature. Their finding was that the 4.1-eV luminescence becomes measureable only for exciting photon energies above 20 eV. They also displayed the fundamental absorption spectrum from 5 to 30 eV. The absorption coefficient shows a monotonic and significant decrease starting from 16 eV and continuing up through the end of measurements at 30 eV. Belsky *et al.* interpreted the 20-eV excitation threshold for appearance of 4.1-eV luminescence at room temperature as evidence against its identification with self-trapped exciton luminescence. They suggested instead that the 4.1-eV luminescence comes from a transient defect or defect complex created by the excitation photons [70].

As noted earlier, Nishimura *et al.* [36] were able to excite the 4.1-eV band with 6.36-eV excitation that penetrated well below the surface due to its two-photon nature. If one insists that the only difference in the two experiments is the energy of the excitation (6.36 and $>$20 eV, respectively), then we have a contradiction not just between interpretations, but between experimental findings. However, if the difference is the depth of excitation below the surface, then the two experiments might be reconciled in principle. The relation of the experimental findings of Belsky *et al.* versus Nishimura *et al.* could be qualitatively the same as that between the experimental findings of Kubota *et al.* versus Nishimura *et al.*, which was already commented on in Ref. [36].

In summary, we have the situation that one of the main luminescence bands whose contribution to scintillation response is being modeled in this paper has two competing interpretive attributions dating from the same 1994-95 time period and published in the same journal. For the reasons outlined briefly above, particularly that 4.1-eV fast intrinsic room-temperature luminescence of CsI has been observed with 6.36-eV excitation [36], and because the Nishimura equilibrating on-center/off-center STE model provides a basis for analyzing temperature-dependent radiative and nonradiative rate constants $R_{1E}(T)$ and $K_{1E}(T)$ needed in the present modeling, we have adopted the Nishimura *et al.* STE model for fast intrinsic room-temperature luminescence of CsI as the working hypothesis for undoped CsI luminescence and scintillation in the present work.

APPENDIX B: MEASURED GAMMA RESPONSE OF UNDOPED AND TL-DOPED CsI; COMPARISON TO ELECTRON RESPONSE

As already pointed out, the model under study calculates electron response, not gamma response. The room-temperature measurements used are Compton-coincidence electron response but the 100 K data available so far are gamma response. For this reason we also measured the gamma response of the undoped and Tl-doped samples used for the room temperature curves. Results are shown in Fig. 11. The upper pair of curves in the figure compare the undoped electron response with the undoped gamma results. This pair is offset 0.1 vertically for display purposes. The results for the Tl-doped sample's electron response and gamma results are shown in the lower curves, which are not offset. The final curve (* symbols) shown with the lower group is the room temperature gamma results for Tl-doped CsI extracted from Moszynski *et al.* [26]. Before the offsets for display purposes all data sets pass through the normalized value of 1.0 at 662 keV.

From Fig. 11, we see that the gamma response curve resembles electron response, but the features (rises, falls, humps) are shifted roughly 10 to 20 keV to higher gamma energy compared to electron energy. This is expected because the gamma event can include multiple lower-energy electrons from Compton scatter, as well as escape of some scattered gammas.

With these things in mind an experimental electron response curve at 100 K could be expected to occur somewhat to the left of the gamma response experiment shown in Fig. 5.

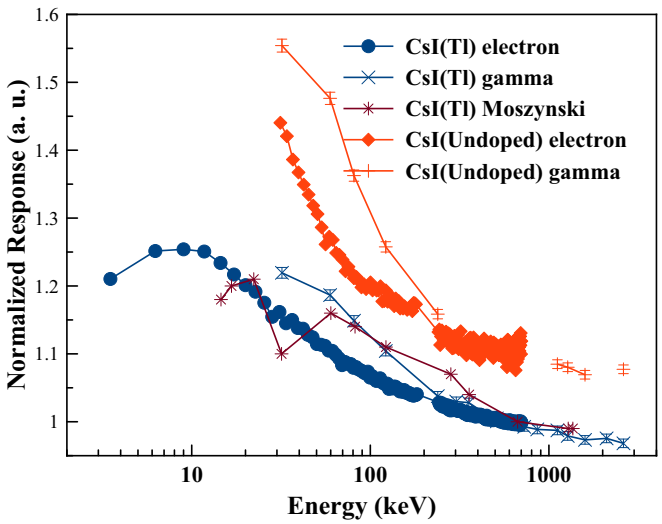

FIG. 11. (Color online) Five room-temperature CsI proportionality curves are displayed. The lower one marked with solid circles is the electron response of CsI(Tl) while the one marked with solid diamonds is the electron response of undoped CsI after a 0.1 vertical offset to separate the display. Each is accompanied by the measured gamma response of the same sample with the undoped curve again offset by 0.1. The fifth curve marked with * is the room-temperature gamma response curve for CsI(Tl) extracted from Moszynski *et al.* [26].

APPENDIX C: CHARACTERIZATION OF UNDOPED CsI

The so-called pure CsI scintillator finds application at room temperature because of its short decay time of about 15 ns, despite its low light output. This fast, intrinsic luminescence is usually accompanied by some amount of slower defect related emission. The fast signal emits in a band near 310 nm in the ultraviolet (uv) and is attributed to recombination of self-trapped excitons (STE) in a thermally equilibrated population of on-center and off-center STEs [36]. Slow signals occur in or near the visible (especially around 425 nm) and are associated with defects in the crystal structure such as impurities or vacancies or combinations of these [41,42]. The quality of the material is often specified by the fast to total luminescence ratio. Another related indicator is the amount of visible radio-luminescence compared to the 310-nm band emission. Moszynski and colleagues published the radioluminescence spectra of their samples with Am-241 gamma excitation.

The radioluminescence of the undoped SGC sample in this study was measured similarly using a Cary Eclipse fluorescence spectrophotometer with the sample placed against the entrance slit to the analysis section, which was opened to the maximum available width (5-nm pass band) to increase signal level. To further improve the signal, 20 scans were summed. In addition to radioluminescence, decay time characteristics were also measured to determine the fast to total ratio. We examined the sample further by conducting an impurity analysis and by measuring the optical absorption in the spectral range where optically active trace impurities such as Tl would absorb. We turn our attention first to the radioluminescence.

The lower three curves in Fig. 12 show results for CsI(A) (solid circles) and CsI(B) (solid diamonds) from Moszynski *et al.* [26] together with the spectrum (line) for our undoped CsI sample labeled SGC. These are the same data presented in Fig. 2 of the body of this paper but plotted here versus energy rather than wavelength to facilitate symmetric Gaussian band fitting. The SGC data were shifted 5 nm so that the curve overlaps the CsI(B) curve in the uv and all the data are recast for display against photon energy. All the curves are normalized to unity at the 4-eV band peak. The SGC line is noisy because the signal levels are low and the signal is reported in 1-nm increments.

The CsI(A) and CsI(B) curves are marked at energies corresponding to the 10-nm steps reported in Ref. [26]. Samples CsI(A) and CsI(B) show the dominant STE UV emission peaking at 4.0 eV and they show an additional band sometimes ascribed to vacancies [41,42] peaking near 3 eV but with differing heights relative to the UV band. A single Gaussian band centered at 4.0 eV and another centered at 2.95 eV account for the total emission of the two samples as the fit curves in the middle of Fig. 12 demonstrate.

The curves at the top level in Fig. 12 show a Gaussian three-band fit for CsI(SGC). The 4-eV band for the STE uv emission and the 2.95-eV band attributed to defects involving anion vacancies [41,42] are the same in peak energy and width (0.75 eV FWHM) for all three samples. The long-wavelength band at 2.32 eV (535 nm) has a width of 0.65 eV. The small discrepancy near 2 eV is attributed to second-order spectrum from the 4-eV band. A summary of the fit parameters is

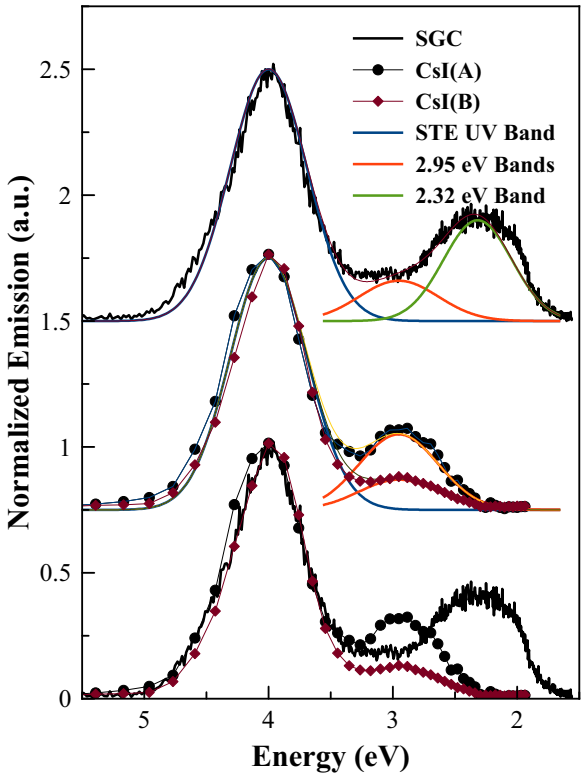

FIG. 12. (Color online) The lower trio of curves, baseline zero, display radioluminescence excited with Am-241 gammas in undoped CsI at room temperature. The solid line labeled SGC is the sample used in this work, the black curve marked with solid circles is sample CsI(A), and the curve marked with solid diamonds is sample CsI(B) whose proportionality is also fit herein. The band-fitted curves are redisplayed with 0.75 and 1.5 signal offsets for band fit illustration (see text). Data for samples CsI(A) and CsI(B) are extracted from Moszynski *et al.* [26].

presented in Table IV. However, extended effort to fit the response with such bands is problematic because neither data set is corrected for the system response and both are known to be falling off into the red. The PMT in the Cary Eclipse instrument has response to 800 nm, whereas the response of the XP2020Q PMT used in Ref. [26] ends at about 600 nm.

These fitting results suggest anion vacancy emissions as a ratio to 4-eV STE emission of 0.12 for CsI(B), 0.16 for the CsI(SGC) sample and 0.30 for CsI(A). Supposing that the area of the 4-eV and 3-eV emissions represent fast and slow signals, respectively, the fast to total ratios can be calculated from the

TABLE IV. Table of band fit parameters Fig. 12.

Peak Parameters	STE UV	Vacancy	SGC Red
Center	4.0 eV	2.95 eV	2.32 eV
FWHM	0.73 eV	0.75 eV	0.65 eV
Peak Heights			
UV	1.0		
CsI(A)		0.30	
CsI(B)		0.12	
SGC Red		0.16	0.40

TABLE V. Chemical analysis of the undoped CsI sample by inductively coupled plasma-mass spectrometry.

Elem	Mol%	Elem	Mol%	Elem	Mol%
Ag	<0.0005%	Cu	<0.0005%	S	<0.001%
Al	<0.0005%	Fe	0.003%	Si	<0.005%
As	<0.005%	K	<0.005%	Sr	<0.0005%
B	<0.0005%	La	<0.0005%	Ti	<0.0005%
Ba	<0.0005%	Li	<0.0005%	Tl	<0.0005%
Be	<0.0005%	Mg	<0.0005%	V	<0.005%
Bi	<0.0005%	Mn	<0.0005%	W	<0.0005%
Ca	<0.005%	Mo	<0.0005%	Zn	<0.0005%
Cd	<0.0005%	Ni	<0.0005%	Zr	<0.0005%
Co	<0.0005%	P	<0.005%		
Cr	<0.0005%	Pb	<0.0005%		

band areas as 76% for CsI(A), a typical value, and 89% for CsI(B) an exceptionally good value. For the SGC sample, the result is 86% if only the 3-eV band is included in the slow signal but this drops to 66% if both bands contribute to the slow signal.

Scintillation decay constants of CsI(SGC) were measured using the Bollinger-Thomas method [72]. The decay constants are 19.9 ns (74.0%) + 1.53 μs (26.0%), where the numbers in parentheses are the fraction of total light yield in the stated component. This leads to a fast to total ratio of 74%, which is typical for undoped CsI from this source. In view of the discussion of band areas above, the result also indicates that some of the long-wavelength (535-nm) emission is included in the 1.53-μs slow component. The estimate of 2.4 times more slow or vacancy component in CsI(SGC) compared to CsI(B) mentioned in the discussion of Table II is based on this comparison of fast to total ratios (75% versus 88%).

Others investigating undoped CsI have come across red emission reminiscent of that seen in sample SGC and ascribe it to Tl contaminants present in manufacturing facilities but without providing direct evidence [56]. We too considered this possibility. First, an impurity analysis was performed with results summarized in Table V. The table

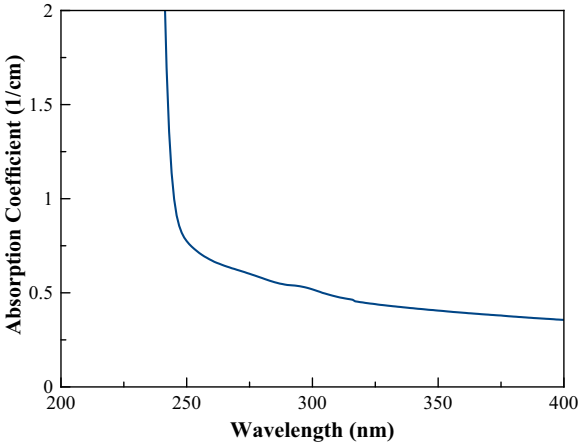

FIG. 13. (Color online) Spectrum of the optical absorption coefficient (cm^{-1}) of the undoped CsI sample (SGC) at room temperature.

shows a chemical analysis for 31 elements performed by inductively coupled plasma-mass spectrometry (ICP-MS) on a slice taken from one end of the sample. Only iron at 0.003% was detected. Tl was <0.0005%. Sodium was not tested.

Optical absorption was examined on the undoped CsI sample to look further for evidence of impurities, with Tl particularly in mind. A portion of the largely structureless spectrum is shown in Fig. 13, Appendix C.

The hint of a small absorption band just below 300 nm is estimated as 0.02 cm^{-1} above the baseline. Using data of Gwin and Murray [38] relating uv absorption to reported Tl concentration of 20 ppm in one of their samples, we estimate that an absorption coefficient of 0.02 cm^{-1} in the SGC sample would correspond to about 0.1 ppm (0.00001 mole%) if it is attributable to Tl. As mentioned, others [56] have attributed unintended luminescence around 535 nm in nominally pure CsI to Tl contamination, but Hamada *et al.* [65] have shown that Tl levels of 1 ppm do not lead to this emission. The defects emitting at 425 nm and 535 nm, together with others that do not emit light, were approximated in our model as one deep trap whose capture rate constant (proportional to concentration and cross section) is treated as a fitting parameter.

[1] W. W. Moses, G. A. Bizarri, R. T. Williams, and S. A. Payne, IEEE Trans. Nucl. Sci. **59**, 2038 (2012).

[2] S. A. Payne, W. W. Moses, S. Sheets, L. Ahle, N. J. Cherepy, B. Sturm, and S. Dazeley, IEEE Trans. Nucl. Sci. **58**, 3392 (2011).

[3] I. V. Khodyuk and P. Dorenbos, IEEE Trans. Nucl. Sci. **59**, 3320 (2012).

[4] J. E. Jaffe, D. V. Jordan, and A. J. Peurrung, Nucl. Instrum. Methods Phys. Res., Sect. A **570**, 72 (2007).

[5] B. D. Rooney and J. D.Valentine, IEEE Trans. Nucl. Sci. **43**, 1271 (1996).

[6] S. A. Payne, N. J. Cherepy, G. Hull, J. D. Valentine, W. W. Moses, and W.-S. Choong, IEEE Trans. Nucl. Sci. **56**, 2506 (2009).

[7] I. Khodyuk, P. A. Rodnyi, and P. Dorenbos, J. Appl. Phys. **107**, 113513 (2010).

[8] K. B. Ucer, G. Bizarri, A. Burger, A. Gektin, L. Trefilova, and R. T. Williams, Phys. Rev. B **89**, 165112 (2014).

[9] J. Q. Grim, K. B. Ucer, A. Burger, P. Bhattacharya, E. Tupitsyn, E. Rowe, V. M. Buliga, L. Trefilova, A. Gektin, G. A. Bizarri, W. W. Moses, and R. T. Williams, Phys. Rev. B **87**, 125117 (2013).

[10] Z. Wang, Y. Xie, L. W. Campbell, F. Gao, and S. Kerisit, J. Appl. Phys. **112**, 014906 (2012).

[11] M. P. Prange, L. W. Campbell, D. Wu, F. Gao, and S. Kerisit, Phys. Rev. B **91**, 104305 (2015).

[12] F. Gao, Y. Xie, S. Kerisit, L. W. Campbell, and W. J. Weber, Nucl. Instrum. Methods Phys. Res., Sect. A **652**, 564 (2011).

[13] G. Bizarri, W. Moses, J. Singh, A. Vasil'ev, and R. Williams, J. Appl. Phys. **105**, 044507 (2009).

[14] R. Kirkin, V. Mikhailin, and A. Vasil'ev, IEEE Trans. Nucl. Sci. **59**, 2057 (2012).

[15] A. Kozorezov, J. K. Wigmore, and A. Owens, J. Appl. Phys. **112**, 053709 (2012).

[16] Q. Li, J. Q. Grim, R. T. Williams, G. A. Bizarri, and W. W. Moses, J. Appl. Phys. **109**, 123716 (2011).

[17] Q. Li, J. Q. Grim, K. B. Ucer, A. Burger, G. A. Bizarri, W. W. Moses, and R. T. Williams, Phys. Status Solidi RRL **6**, 346 (2012).

[18] A. N. Vasil'ev and A. V. Gektin, IEEE Trans. Nucl. Sci. **61**, 235 (2014).

[19] R. T. Williams, J. Q. Grim, Q. Li, K. B. Ucer, and W. W. Moses, Phys. Status Solidi B **248**, 426 (2011).

[20] J. Q. Grim, Q. Li, K. B. Ucer, A. Burger, G. A. Bizarri, W. W. Moses, and R. T. Williams, Phys. Status Solidi A **209**, 2421 (2012).

[21] Q. Li, X. Lu, and R. T. Williams, in *Proceedings SPIE Symposium on Hard X-Ray, Gamma-Ray, and Neutron Detectors, SPIE Vol. 9213, 92130K-1* (2014).

[22] F. Gao, Y. Xie, Z. Wang, S. N. Kerist, L. W. Campbell, R. M. V. Ginhoven, and M. P. Prange, presented in Symposium on Radiation Measurements and Applications, SORMA (Oakland, CA) (2012) (unpublished).

[23] F. Gao, Y. Xie, Z. Wang, S. Kerisit, D. Wu, L. Cambell, R. M. Van Ginhoven, and M. Prange, J. Appl. Phys. **114**, 173512 (2013).

[24] S. Agostinelli *et al.*, Nucl. Instrum. Meth. A **506**, 250 (2003).

[25] J. Allison *et al.*, IEEE Trans. Nucl. Sci. **53**, 270 (2006).

[26] M. Moszynski, M. Balcerzyk, W. Czarnacki, M. Kapusta, W. Klamra, A. S. P. Schotanus, M. Szawlowski, and V. Kozlov, Nucl. Instrum. Methods A **537**, 357 (2005).

[27] J. Q. Grim, Q. Li, K. Ucer, R. Williams, G. Bizarri, and W. Moses, MRS Commun. **2**, 139 (2012).

[28] K. S. Song and R. T. Williams, *Self-trapped Excitons*, Series in Solid State Sciences Vol. 105 (Springer, Heidelberg, 1996).

[29] T. Sugiyama, H. Fujiwara, T. Suzuki, and K. Tanimura, Phys. Rev. B **54**, 15109 (1996).

[30] D. Åberg and B. Sadigh (private communication).

[31] H. B. Dietrich, A. E. Purdy, R. B. Murray, and R. T. Williams, Phys. Rev. B **8**, 5894 (1973).

[32] R. G. Kaufman, W. B. Hadley, and H. N. Hersh, IEEE Trans. Nucl. Sci. **17**, 82 (1970).

[33] A. McAllister, D. Åberg, A. Schleife, and E. Kioupakis, Appl. Phys. Lett. **106**, 141901 (2015).

[34] S. Kerisit, K. M. Rosso, and B. D. Cannon, IEEE Trans. Nucl. Sci. **55**, 1251 (2008).

[35] F. J. Keller and R. B. Murray, Phys. Rev. **150**, 670 (1966).

[36] H. Nishimura, M. Sakata, T. Tsujimoto, and M. Nakayama, Phys. Rev. B **51**, 2167 (1995).

[37] G. W. Rechtenwald, "Finite-difference approximations to the heat equation", (2011), citeSeerX.ist.psu.edu/doi=10.1.1.408.4054.

[38] R. Gwin and R. B. Murray, Phys. Rev. **131**, 501 (1963).

[39] S. Donnald, Ph.D. thesis, University of Tennessee, Knoxville, 2014 .

[40] P. B. Ugorowski, M. J. Harrison, and D. S. McGregor, Nucl. Instrum. Meth. A **615**, 182 (2010).

[41] P. Schotanus, R. Kamermans, and P. Dorenbos, IEEE Trans. Nucl. Sci. **37**, 177 (1990).

[42] L. N. Shpilinskaya, B. G. Zaslavsky, L. V. Kovaleva, S. I. Vasetsky, A. M. Kudin, A. I. Mitichkin, and T. A. Charkina, Semiconductor Phys. Quantum Electron. Optoelectron. **3**, 178 (2000).
[43] D. Fröhlich, B. Staginnus, and Y. Onodera, Phys. Status Solidi **40**, 547 (1970).
[44] W. Martienssen, J. Phys. Chem. Solids **2**, 257 (1957).
[45] R. C. Alig and S. Bloom, J. Appl. Phys. **49**, 3476 (1978).
[46] P. Dorenbos, IEEE Trans. Nucl. Sci. **57**, 1162 (2010).
[47] Z. Wang, Y. L. Xie, B. D. Cannon, L. W. Campbell, F. Gao, and S. Kerisit, J. Appl. Phys. **110**, 064903 (2011).
[48] H. Li, J. Phys. Chem. Ref. Data **5**, 329 (1976).
[49] B. P. Aduev, E. D. Aluker, G. M. Belokurov, and V. N. Shvayko, Phys. Status Solidi B **208**, 137 (1998).
[50] P. Erhart, A. Schleife, B. Sadigh, and D. Åberg, Phys. Rev. B **89**, 075132 (2014).
[51] http://www.crystals.saint-gobain.com/uploadedFiles/SG-Crystals/Documents/CsI Pure Data Sheet.pdf.
[52] R. T. Williams, J. Q. Grim, Q. Li, K. B. Ucer, G. A. Bizarri, S. Kerisit, F. Gao, P. Bhattacharya, E. Tupitsyn, E. Rowe, V. M. Buliga, and A. Burger, in *SPIE Conference Proceedings 8852-20 V. 8 (August 2013)* (2013).
[53] R. T. Williams, J. Q. Grim, Q. Li, K. B. Ucer, G. A. Bizarri, and A. Burger, " Scintillation detectors of radiation: Excitations at high densities and strong gradients", in *Excitonic and Photonic Processes in Materials*, Series in Materials Science, Vol. 203, edited by J. Singh and R. T. Williams (Springer, Singapore, 2014) Chap. 10 .
[54] A. Vasil'ev and A. Gektin, in *Proceedings of the 8th International Conference on Inorganic Scintillators and their Applications (SCINT2005)*, edited by A. Nekton and B. Grinyov (National Academy of Sciences of Ukraine, Kharkov, 2006), pp. 1–6.
[55] C. Amsler, D. Grögler, W. Joffrain, d. Lindelöf, M. Marchesotti, P. Niederberger, H. Pruys, C. Regenfus, P. Riedler, and A. Rotondi, Nucl. Instr. Meth. A **A480**, 494 (2002).
[56] V. B. Mikhailik, V. Kapustyanyk, V. Tsybulskyi, V. Rudyk, and H. Kraus, Phys. Status Solidi **252**, 804 (2015).
[57] K. B. Ucer and R. T. Williams (unpublished).
[58] A. N. Vasil'ev, presented in International Conference on Excitonic Processes in Condensed Matter, EXCON2010 (Darwin, 2010) (unpublished).
[59] R. B. Murray and A. Meyer, Phys. Rev. **122**, 815 (1961).
[60] R. K. Ahrenkiel and F. C. Brown, Phys. Rev. **136**, A223 (1964).
[61] Z. Wang, R. T. Williams, J. Q. Grim, F. Gao, and S. Kerisit, Phys. Status Solidi B **250**, 1532 (2013).
[62] A. Alkauskas, Q. Yan, and C. G. Van de Walle, Phys. Rev. B **90**, 075202 (2014).
[63] M. Kirm, V. Nagirnyi, E. Feldbach, M. DeGrazia, B. Carre, H. Merdji, S. Guizard, G. Geoffroy, J. Gaudin, N. Fedorov, P. Martin, A. Vasil'ev, and A. Belsky, Phys. Rev. B **79**, 233103 (2009).
[64] A. Alkauskas, presented in International Conference on Inorganic Scintillators and their Applications, SCINT2015, Berkeley, June 7-12 (2015) (unpublished).
[65] M. M. Hamada, F. E. Costa, M. C. C. Pereira, and S. Kubota, IEEE Trans. Nucl. Sci. **48**, 1148 (2001).
[66] S. Gridin, Ph.D. thesis, Universite Claude Bernard Lyon 1, 2014.
[67] A. Syntfeld-Kazuch, L. Swiderski, and M. Moszynski, *Conference Record, IEEE Nuclear Science Symposium and Medical Imaging Conference (NSS-MIC)* (Seattle, WA, Nov. 8-15, 2014) PID3497813-NSSMIC14.
[68] A. Syntfeld-Kazuch, M. Moszynski, L. Swiderski, W. Klamra, and A. Nassalski, IEEE Trans. Nucl. Sci. **55**, 1246 (2008).
[69] J. D. Valentine, W. W. Moses, S. E. Derenzo, D. K. Wehe, and G. F. Knoll, Nucl. Instrum. Meth. A **325**, 147 (1993).
[70] A. N. Belsky, A. N. Vasil'ev, V. V. Mikhailin, A. V. Gektin, P. Martin, C. Pedrini, and D. Bouttet, Phys. Rev. B **49**, 13197 (1994).
[71] S. Kubota, S. Sakuragi, S. Hashimoto, and J. Ruan, Nucl. Instrum. Methods A **268**, 275 (1988).
[72] L. M. Bollinger and G. E. Thomas, Rev. Sci. Instrum. **32**, 1044 (1961).